

Nonlinear Optical Spectroscopic Study of Topological Weyl Semimetals

A Thesis submitted to

**Indian Institute of Science Education and Research,
Pune**

in partial fulfilment of the requirements for the BS-MS Dual Degree Programme

by

Ziyad Thekkayil

(Reg. No: 20181139)



Indian Institute of Science Education and Research Pune

Dr. Homi Bhabha Road,
Pashan, Pune 411008, INDIA.

Supervisor: **Prof. Eric Borguet**

Temple University, Philadelphia, USA

*Dedicated to my mother and my sister, who held my fingers as I took my first
steps in life and science...*

CERTIFICATE

This is to certify that this dissertation entitled “**Nonlinear Optical Spectroscopic Study of Topological Weyl Semimetals**” towards the partial fulfilment of the BS-MS dual degree programme at the Indian Institute of Science Education and Research, Pune represents study/work carried out by **Ziyad Thekkayil** at Temple University under the supervision of **Prof. Eric Borguet**, Professor of Chemistry, College of Science and Technology, Temple University, Philadelphia, USA during the academic year 2022-23.

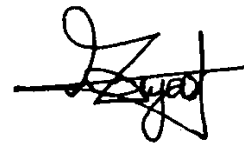


Prof. Eric Borguet

10 May 2023

DECLARATION

I hereby declare that the matter embodied in the report entitled “**Nonlinear Optical Spectroscopic Study of Topological Weyl Semimetals**” are the results of the work carried out by me at the Department of Chemistry, College of Science and Technology, Temple University, under the supervision of Prof. Eric Borguet and the same has not been submitted elsewhere for any other degree.

A handwritten signature in black ink, appearing to read 'Ziyad', with a horizontal line drawn through it.

Ziyad Thekkayil

10 May 2023

Acknowledgements

It's very difficult for me to accept that my stay at IISER Pune has come to an end. IISER has been a safe haven and a second home for me over the past few years. I want to thank everyone who was part of my journey and made my life eventful.

Firstly, I would like to thank my advisor Dr. Eric Borguet, who constantly motivates me to not only be a better researcher, but also to be a better version of myself. I am highly thankful to him for deeming me capable of joining as a graduate student in his group during the 4th year of my BSMS. Working with him during the past year has been an exciting learning experience. He has been a great mentor and a helping hand, even for activities outside of academics and research. I look forward to the remaining years of my PhD under him with excitement and hope.

I would also like to sincerely thank my co-advisor Dr. Pankaj Mandal, who was also my supervisor for more than 3 years during my undergraduate research at IISER. I am immensely grateful to him for allowing me to work with him right from my 1st year, and for providing me guidance with research and coursework, as well as the difficulties I faced during my stay at IISER. Thanks to him, I could spend the time after the lockdown entirely on research. I had the freedom to walk into his office anytime and bother him with my doubts and problems. I hope to have more collaborative works with him in the future.

I express my gratitude to my TAC member Dr. Pramod Pillai for providing valuable feedback for my MS project. I would also like to thank him and Dr. Partha Hazra for providing me with valuable recommendation letters for my PhD admission, and the coordinator of DMDD Dr. Ramanathan Vaidyanathan, for helping me with the admission.

I am grateful to my collaborators during the MS project Dr. Daniel Strongin, Benjamin and Uddipana from Temple University, and Dr. Steven May and Prajwal from Drexel University, for providing us with samples and for the valuable discussions. I am grateful to Amudhan from the Borguet group for performing the STM measurements.

I am highly grateful to my senior lab mates at Dr. Mandal's lab Sneha, Avinash, Shabnum, Aman and Rapti, for nurturing the scientific passion in me and helping me to grow as an independent researcher. Riteeka, Chandan, Garvit and Nandana have been amazing colleagues. I thank you all for providing a good work environment.

I want to express my immense gratitude to my seniors in Dr. Borguet's NLO group Somaiyeh, Bijoya and Joy, for constantly mentoring and guiding me throughout. Your help has been invaluable in completing my MS project. I would also like to thank the other members of the Borguet group for their valuable suggestions and feedback.

I am highly indebted to Tariq, Shabnum, and Bharath for standing with me through all my ups and downs. You have become inseparable from my life. I also want to thank all my friends who constantly supported me and gave me wonderful memories. I cannot proceed without mentioning Saleem, Riteeka, Pranav and Aby. Thank you so much for giving company to that silent kid who rarely made any friends. I would also like to especially thank my friends from the 3rd floor of IISER PhD hostel. The cooking and chat sessions with you were wonderful. I have spent more time in the PhD hostel than in the BSMS hostel due to the wonderful friendship and care that you have provided. Also, as someone who had to change rooms almost every year, I got to be with multiple roommates. I am grateful to them all for providing me with a friendly and supportive environment, especially to my current roommates Sanjay, Vaibhav and Amudhan, for their constant support and valuable scientific discussions.

I cannot express in words my gratitude to my family, especially my parents, Ayishabi A.K. and Mohiyuddin Firdouse. They have endured great hardships in life. I believe beyond doubt that it's my mother's prayers that keep me going at my most difficult moments. My uncle Ismayil T. has also been a parental figure in my life, and I am highly indebted to him for everything I have achieved.

All my teachers during my school life, IISER and outside, had a significant role in motivating me to pursue a research career. I would like to specially mention my higher secondary teacher Mr. M.T. Javad, who always encouraged me to think critically and seek knowledge beyond what is provided. As rightly put by one of my heroes Dr. Brian Green, "My best teachers were not the ones who knew all the answers, but those who were deeply excited by questions they couldn't answer."

I would like to thank DST Inspire and the Infosys Foundation for providing me with scholarships which proved essential during my IISER life, and the Department of Chemistry, Temple University, for the fellowship during my MS thesis. Last but not the least, I want to thank all the faculty and staff for making IISER a wonderful place.

Table of Contents

Abstract	1
1. Introduction	2
1.1 Topological Materials	2
1.2 Identification of Topological Materials	3
1.3 Nonlinear Optical Spectroscopy	4
1.4 Scope of This Thesis	6
2. Experimental Methods.....	8
2.1 Samples.....	8
2.2 Raman Microscopy	8
2.3 X-Ray Diffraction (XRD).....	8
2.4 Scanning Tunneling Microscopy (STM)	8
2.5 Atomic Force Microscopy (AFM).....	8
2.6 Second Harmonic Generation.....	9
3. Results and Discussion	12
3.1 Characterization.....	12
3.1.1 Optical Microscopy and Raman Spectroscopy of Td-WTe ₂	12
3.1.2 Optical Characterization of Mn ₃ Sn/LaAlO ₃ Thin Film	13
3.1.2 X-Ray diffraction spectrum of Mn ₃ Sn/LaAlO ₃ Thin Film	13
3.1.3 AFM Image of Td-WTe ₂ /Si Thin Film	14
3.1.4 STM Image of Td-WTe ₂ Single Crystal.....	15
3.2 Wavelength and Polarization Dependent SHG from WTe ₂ and Mn ₃ Sn.....	16
3.2.1 SHG in PP Geometry.....	17
3.2.2 SHG in SP Geometry.....	21

3.3 SHG from Td-WTe ₂ Single Crystal.....	23
3.4 Stability During SHG Experiments	24
3.4.1 Power Dependence of SHG.....	24
3.4.2 SHG Output vs Time.....	25
3.4.3 SHG Dependence on Laser Repetition Rate	26
4. Thesis Summary and Future Outlook.....	28
Appendix	30
A1. Studying the Stability During Electrochemical Activity	30
A2. Automation of Delay Stage via LabVIEW	32
A3. Calculation of Beam Diameters	33
A4. Wavelength Dependent Efficiency Curve of CCD and Grating.....	36
References.....	37

List of Figures

Figure 1.1. Band Diagram	3
Figure 1.2. Second Harmonic Generation	5
Figure 1.3. Second Harmonic Generation from Interface	6
Figure 2.1. SHG Experimental Setup	9
Figure 2.2. Beam Diameter Before the Focusing Lens	10
Figure 2.3. Beam Diameter at the Sample Position	11
Figure 3.1. Optical Characterization of Td-WTe ₂	12
Figure 3.2. Optical Characterization of Mn ₃ Sn	13
Figure 3.3. PXRD Spectra	14
Figure 3.4. AFM Image of Td-WTe ₂ /Si Thin Film	15
Figure 3.5. STM Image of Td-WTe ₂ Single Crystal	15
Figure 3.6. Schematic of area illuminated	17
Figure 3.7. SHG PP Response of Td-WTe ₂ /Si	18
Figure 3.8. PP-SHG Response of Td-WTe ₂ /Si and Mn ₃ Sn/LaAlO ₃ thin films	20
Figure 3.9. PP-SHG Response of Td-WTe ₂ /Si and Mn ₃ Sn/LaAlO ₃ thin films	21
Figure 3.10. Normalized SP-SHG Spectra of Td-WTe ₂ /Si & Mn ₃ Sn/LaAlO ₃ thin films	22
Figure 3.11. Comparison of SP and PP SHG Intensity of Si	23
Figure 3.12. SHG From Td-WTe ₂ Single Crystal	24
Figure 3.13. Power Dependence of SHG	25
Figure 3.14. SHG vs Time	25
Figure 3.15. Dependence of SHG Output on Laser Repetition Rate	27
Figure A1.1. Raman Spectra after Electrochemical Activity	31

Figure A2.1. LabVIEW Program.....	32
Figure A3.1. Knife-Edge Technique	33
Figure A4.1. Quantum Efficiency of CCD	36
Figure A4.2. Efficiency of Diffraction Grating.....	36

Abstract

Topological Weyl semimetals demonstrate interesting properties like exotic surface fermi arcs and chiral Weyl points, making them a strong candidate for many potential applications in electronics, optoelectronics, and catalysis. However, currently, their identification requires demanding experimental conditions like low temperatures or ultrahigh vacuum. Hence, there is a need for experimental techniques that can identify their topological states under ambient conditions. Second-order nonlinear optical processes, being sensitive to breaks in symmetries, have the potential to identify topological states. We employed wavelength-dependent reflection SHG measurements to study the surface of thin films of Weyl semimetals Td-WTe₂ and Mn₃Sn. Our studies show some promising results such as the effect of wavelength and polarization geometry in understanding the surface electronic properties of these materials. The systems are also stable to continuous illumination and high power and repetition rates, and do not show any significant heating or charging effects within our experimental conditions.

Chapter 1

Introduction

1.1 Topological Materials

The electronic properties of solids are described by the band theory, which is based on the nearly free electron model.¹ The electrons are considered like gaseous particles in a lattice of weak periodic potential or the Bloch potential.² The Bloch potential assumes the lattice to be continuous and periodic, which is true when we consider the bulk of a solid. However, at the surface of a solid, the periodicity of the lattice breaks, and therefore the electrons close to the surface experience a different environment. This can result in the band structure being different at the surface as compared to the bulk.

Topology is a mathematical concept that deals with smooth deformations and variations of surfaces.³ A class of materials known as topological materials have been an interesting development in condensed matter physics over the past 2 decades. They are characterized by robust surface electronic states distinguished by the notion of topological order; their fundamental properties are insensitive to defects and smooth changes in the material parameters unless there is a quantum phase transition.⁴ Theoretical predictions⁵⁻⁶ of spin-orbit interactions resulting in topological states and their experimental confirmations⁷⁻⁸ have led to the realization of quasiparticle analogues of exotic fermions predicted by the Dirac equation and its variants in particle physics. These materials exhibit inversion of valence and conduction bands and band-crossing points occurring due to spin-orbit coupling (Figure 1.1). This results in them having topological surface states with spin-momentum locking, and ultra-high carrier mobility owing to linear dispersion near the band-crossing points.⁹⁻¹⁰ These interesting properties make them a potential candidate for applications in electronics, optoelectronics, etc.¹¹ Based on the presence or absence of a bandgap in the bulk, topological materials are classified as topological insulators (TI) or topological semimetals, respectively.

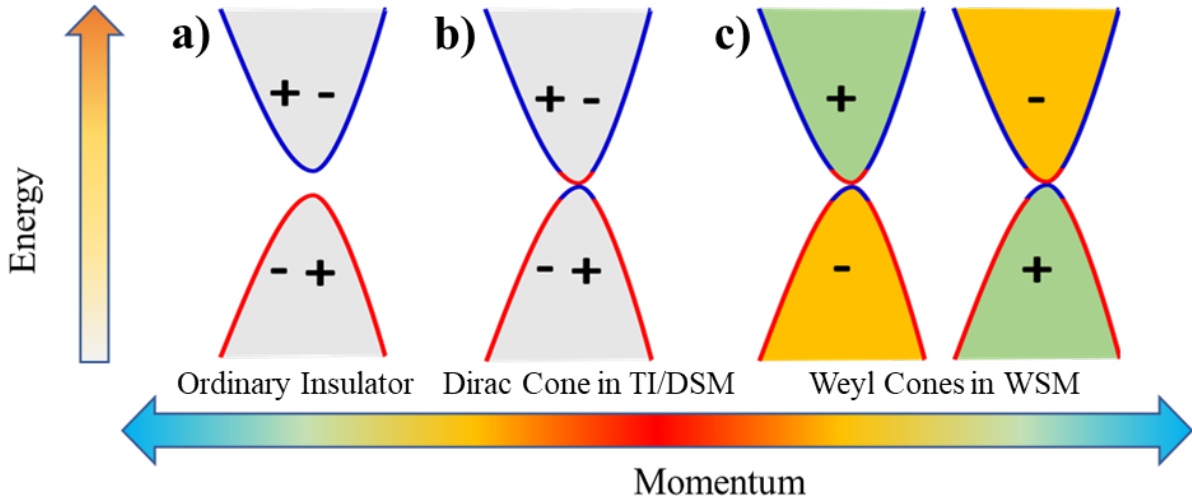


Figure 1.1. Band Diagram: (a) The band diagram of an ordinary insulator. (b) Inversion of bands leading to band crossing points in topological insulators/Dirac semimetals. (c) Splitting of Dirac cones into two Weyl cones of opposite chirality in a Weyl semimetal.

Topological semimetals are further classified as Dirac and Weyl semimetals based on symmetry.¹² Dirac semimetals (DSM) are similar to topological insulators, with band-crossing points, or “Dirac cones”, on the surface. In Weyl semimetals (WSM), the Dirac cones are split into an even number of “Weyl cones” with opposite chirality, due to which they host chiral charge carriers, also known as Weyl fermions.¹³ This splitting of each Dirac cone into Weyl cones of opposite chirality requires that either time reversal or inversion symmetry be broken.¹² Weyl semimetals host exotic metallic surfaces that terminate at the Weyl points, known as “Fermi arcs”. The exotic carrier properties make Weyl semimetals have important applications like spintronics, catalysis, etc.¹⁴ Weyl semimetals are further classified as type-I and type-II based on the amount of tilt of the Weyl cones, with type-II Weyl semimetals having an over tilted Weyl cone.¹⁵

1.2 Identification of Topological Materials

The first step in the identification of topological phases, including Weyl semimetals, is through the *ab initio* theoretical calculations of the band structure.¹⁶ The experimental confirmation of the topological band structure is through techniques that can map the bands or provide some signature of the non-trivial band structure. The current techniques that are used for the experimental confirmation of topological states are

mainly angle-resolved photoelectron spectroscopy¹⁷ (ARPES) and ultrahigh vacuum scanning tunneling microscopy¹⁸ (UHV-STM). However, these techniques require demanding conditions such as extremely low temperatures or ultrahigh vacuum. Quantum transport measurements provide some signature of the topological states¹⁹, but being electrical contact techniques, they are inherently perturbative in nature. In short, currently there are no ambient non-perturbative techniques that can experimentally verify the presence of non-trivial topological states in a material.

1.3 Nonlinear Optical Spectroscopy

Most of the light-matter interactions that we come across routinely fall under linear optics, where the interaction of matter is linearly proportional to the electric field of light. However, at very high light intensities, the nonlinear light-matter interactions come into play. They are governed by the nonlinear polarization equation (equation 1.1), which relates the polarization of material to the magnitude of the electric field:²⁰

$$P(E) = \varepsilon_0 [\chi^{(1)}E + \chi^{(2)}E^2 + \chi^{(3)}E^3 + \dots] \quad (1.1)$$

where $P(E)$ is the polarization induced in the material upon the application of an electric field E , ε_0 is the permittivity of free space, and $\chi^{(n)}$ is the n^{th} order optical susceptibility. The order of an optical process is determined by the total number of waves involved in the process; an n^{th} order process involves $n+1$ waves. The magnitude of the optical susceptibilities typically decreases by many orders of magnitude with increase in the order of the process, and so the magnitude of 'E' has to increase sufficiently high for them to be significant and detectable. For even order nonlinear optical (NLO) processes, the susceptibility vanishes to zero for centrosymmetric and isotropic media due to symmetry conditions. Therefore, even order NLO processes are sensitive to asymmetries or break in symmetries.

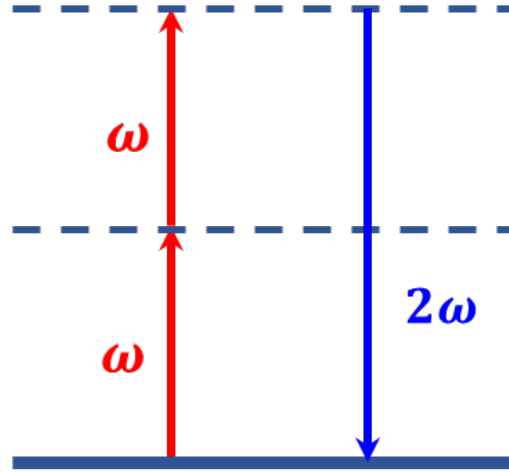


Figure 1.2. Second Harmonic Generation: Two photons of frequency ω polarize the system and excite it into successive virtual states, and the system emits a photon of 2ω while coming back to the initial state.

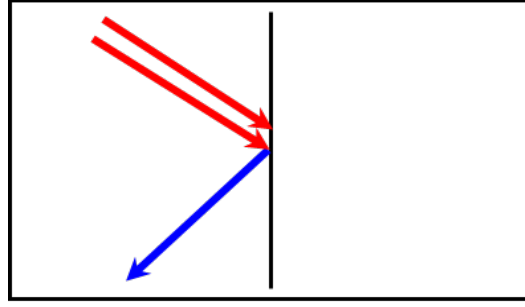
Second harmonic generation (SHG) is a second order NLO process where 2 incident photons of frequency ' ω ' excite the material. The electric field of the photons polarizes the system and takes it into virtual states, and the system then radiates at the second harmonic frequency ' 2ω ' (Figure 1.2). As SHG is an even order process, it is sensitive to breaks in symmetry. Centrosymmetric bulk media have a vanishing $\chi^{(2)}$ and therefore cannot generate an SHG response, within the electric dipole approximation. However, at the surface or an interface, there is a break of symmetry, and therefore SHG can be observed from surfaces and interfaces (Figure 1.3). Hence, SHG can be used as an efficient tool to study surfaces and interfaces.²¹

The SHG response of a material is dependent on the second order polarization at the second harmonic frequency $P_i^{(2)}(2\omega)$;²⁰

$$P_i^{(2)}(2\omega) = \sum_{i,j,k} \chi_{ijk}^{(2)}(2\omega, \omega, \omega) E_j(\omega) E_k(\omega) \quad (1.2)$$

where $\chi_{ijk}^{(2)}$ is the second order NLO susceptibility, E_j and E_k being the incident electric fields, and i, j and k are the cartesian coordinates.

$$P_2 = \chi^{(2)} E_i E_j$$



$$\chi^{(2)} \neq 0$$

Figure 1.3. Second Harmonic Generation from Interface: The $\chi^{(2)}$ is non-zero at surfaces/interfaces in the electric dipole approximation, leading to an SHG response.

The SHG response thus generated due to this polarization from a surface can be described by the equation:²²

$$I(2\omega) = A \cdot \left| \hat{e}_i(2\omega) \chi_{ijk}^{(2)} \hat{e}_j(\omega) \hat{e}_k(\omega) I(\omega) \right|^2 \quad (1.3)$$

where A is a constant determined by the experimental geometry, \hat{e}_i is the polarization vector of the outgoing SHG beam, \hat{e}_j and \hat{e}_k are the polarization vectors of the excitation waves, and $I(\omega)$ is the intensity of the incident beam. So, the SHG response will be dependent on the interaction of the polarizations of the input and the SHG beams with the material properties.

1.4 Scope of This Thesis

As mentioned earlier, there aren't any ambient non-perturbative techniques that can identify non-trivial topological surface states. Visible and IR light are non-invasive tools to study the properties of materials. Since even order NLO processes like SHG are sensitive to surfaces, SHG spectroscopy using Visible and IR light can possibly serve as tool to probe the topological states. Although there are many SHG studies of Weyl semimetals²³, most of them are restricted to studies at single wavelengths. However, only a wavelength dependent SHG spectroscopy can properly map the band energies and carrier transitions within the band structure.

To the best of our knowledge, TaAs²⁴ and RhSi²⁵ are the only Weyl semimetals on which a wavelength dependent SHG spectroscopic study has been performed, which

showed a resonant enhancement of SHG, and its relation to the band geometry. The SHG response from RhSi was observed to be suppressed near the Weyl points. Therefore, it is important to conduct wavelength dependent SHG studies on different Weyl semimetals to have a clear understanding of the effect of topological band structure on the SHG response. If the SHG spectroscopy is able to detect any signatures of the topological states, it can serve as effective ambient technique to identify and understand the topological properties of materials. Therefore, in this thesis, we used SHG spectroscopy to study the surfaces of thin films of 2 topological Weyl semimetals, namely Td-WTe₂, which is material that has 3 different topological phases under different conditions²⁶⁻²⁷, and Mn₃Sn, which is an antiferromagnetic Weyl semimetal that has demonstrated interesting electronic properties like large anomalous hall effect at room temperature.²⁸⁻²⁹ We developed an experimental setup to perform SHG spectroscopy in the reflection geometry from these materials, and studied the SHG response of these systems, by varying the wavelength, polarization geometry, intensity, and laser pulse repetition rates.

Chapter 2

Experimental Methods

2.1 Samples

- (i) Td-WTe₂ thin film on Si substrate was provided by Strongin group, Temple University
- (ii) Td-WTe₂ single crystal from 2DCC-MIP, Penn State University, was obtained via Strongin group, Temple University
- (iii) Mn₃Sn thin film on LaAlO₃ substrate was provided May Group, Drexel University

2.2 Raman Microscopy

A HORIBA LabRAM HR Evolution Raman microscope with variable objective lens of focal lengths 5X/10X/50X/100X was used to obtain the microscopic images and Raman spectrum from the samples. The Raman spectrometer was calibrated with a standard silicon crystal sample using the 520 cm⁻¹ peak. The Raman spectra were collected by focusing on the sample spots, accumulating over 10 scans, and averaging over 10 spectra.

2.3 X-Ray Diffraction (XRD)

The XRD spectra were recorded using a 4-axis Rigaku SmartLab diffractometer with a double bounce Ge-crystal high-resolution monochromator, and Cu-K α radiation of wavelength 1.5406 Angstrom as the excitation source.

2.4 Scanning Tunneling Microscopy (STM)

The STM images were obtained using a PicoScan STM system, with a 1 nA/V preamplifier. The images were recorded at room temperature and ambient pressure.

2.5 Atomic Force Microscopy (AFM)

The AFM images were obtained in ambient conditions using a Veeco Dimension Icon Scanning Probe Microscope with an Sb-doped Si AFM tip having a nominal tip radius of 10 nm. An AC voltage was applied to the z-piezo to drive the oscillation of the

cantilever at its resonance frequency (320 Hz). In order to keep the amplitude constant, a feedback loop was used to fix the tip-sample separation point by point.

2.6 Second Harmonic Generation

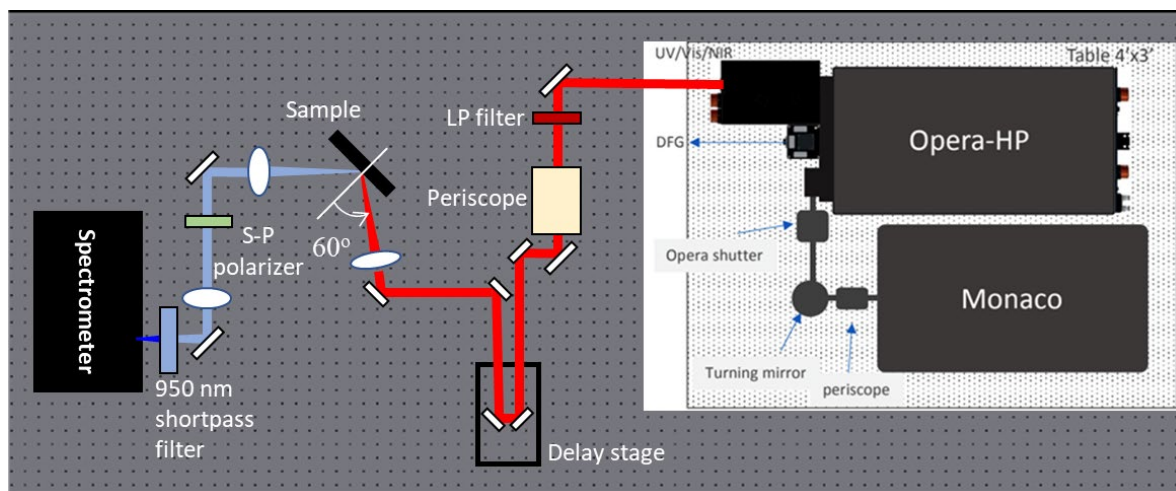


Figure 2.1. SHG Experimental Setup: The samples were excited using NIR light ranging from 1200-1600 nm from the OPA, with an incidence angle of 60° . The SHG output was collected in the reflection geometry.

The SHG experiments were conducted using a 300–4800 nm wavelength-tunable ORPHEUS-HP optical parametric amplifier (OPA, Light Conversion), pumped by a Monaco ultrafast diode-pumped fiber laser (Coherent), generating 400 fs pulses with 1035 nm central wavelength, with a variable pulse repetition rate from 1 Hz to 1 MHz (Figure 2.1). The experiments were performed in the Near Infrared (NIR) idler output wavelength range 1200-1800 nm with a repetition rate of 25 kHz, at constant power of 10 mW. A 1050 nm long pass filter was used to block the fundamental signal wavelengths from reaching the sample. The output polarization of the OPA is vertically polarized, and so a periscope was used to change the polarization to horizontal so that the vertically placed sample is excited by P-polarized light. A variable neutral density (N.D.) filter was used to adjust the power to 10 mW. The beam was passed through a retroreflector attached to a translation stage keeping in mind the possibility of time-resolved measurements in the future. The beam was focused onto the sample using a 150 mm plano-convex lens, at an angle of $\sim 60^\circ$ angle with respect to the surface normal, and the SHG output was collected in the reflection geometry. The output was collimated using a 50 mm plano-convex lens. An S-P polarizer was used

to resolve the polarization of the output. The output was focused on the entrance slit of the spectrometer using a 200 mm plano-convex lens, and a 950 nm short pass filter was used to block the pump beam photons from being detected. The output was recorded using a Princeton SpectraPro HRS-300-S spectrograph with a 300 gr/mm 500 nm blaze i1-030-500-P and PIXIS 1024B CCD.

The profile of the excitation beam at 1200 nm was measured using the knife-edge technique.³⁰ The transmitted power was recorded against the position of the knife-edge while moving the knife-edge along the beam cross section, and the derivative of the transmitted power against the knife-edge position was calculated to reconstruct the Gaussian profile. The $1/e^2$ diameter of the beam before the focusing lens prior to the sample was obtained to be 4.6 mm (Figure 2.2).

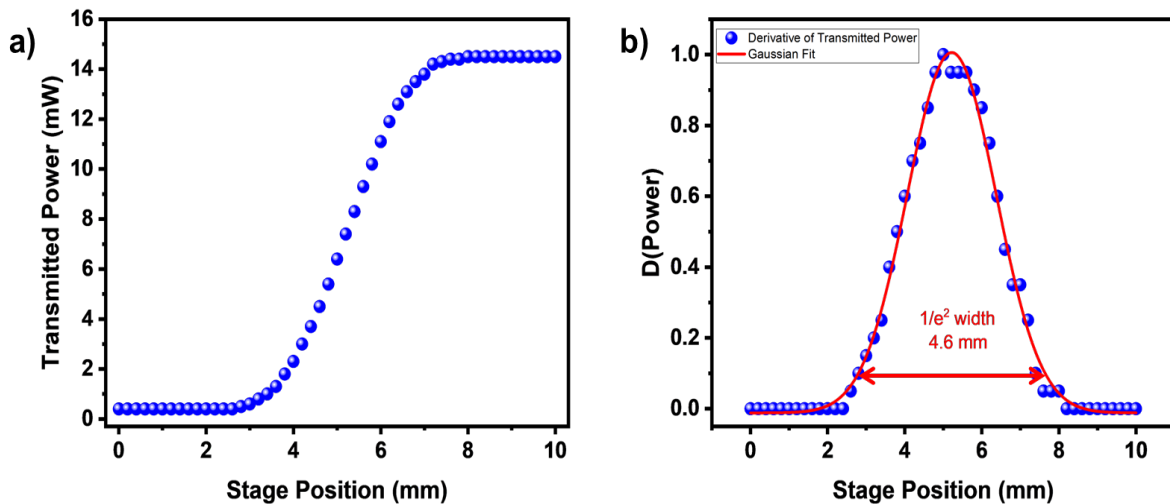


Figure 2.2. Beam Diameter Before the Focusing Lens: (a) Transmitted power against knife-edge position. (b) Gaussian profile reconstructed by taking the derivative of transmitted power.

The theoretical spot size at the focal point was calculated using the equation:³¹

$$2w_0 = \left(\frac{4M^2\lambda}{\pi} \right) \times \left(\frac{F}{D} \right) \quad (2.1)$$

where $2w_0$ is the $1/e^2$ beam diameter at the focal point, M^2 is a parameter that indicates how close the beam is to a perfect Gaussian (with a perfect Gaussian beam having an $M^2 = 1$), λ is the wavelength of light, f is the focal length of the focusing lens, and D is the beam diameter before the lens. Plugging in the values, we get the theoretical

beam diameter at focal point to be $50\ \mu\text{m}$ (see Appendix A3 for the calculations). The beam diameter at the sample position was also measured using the knife-edge technique, and was obtained to be $70\ \mu\text{m}$ (Figure 2.3), thereby giving an M^2 value of 1.4 for the beam.

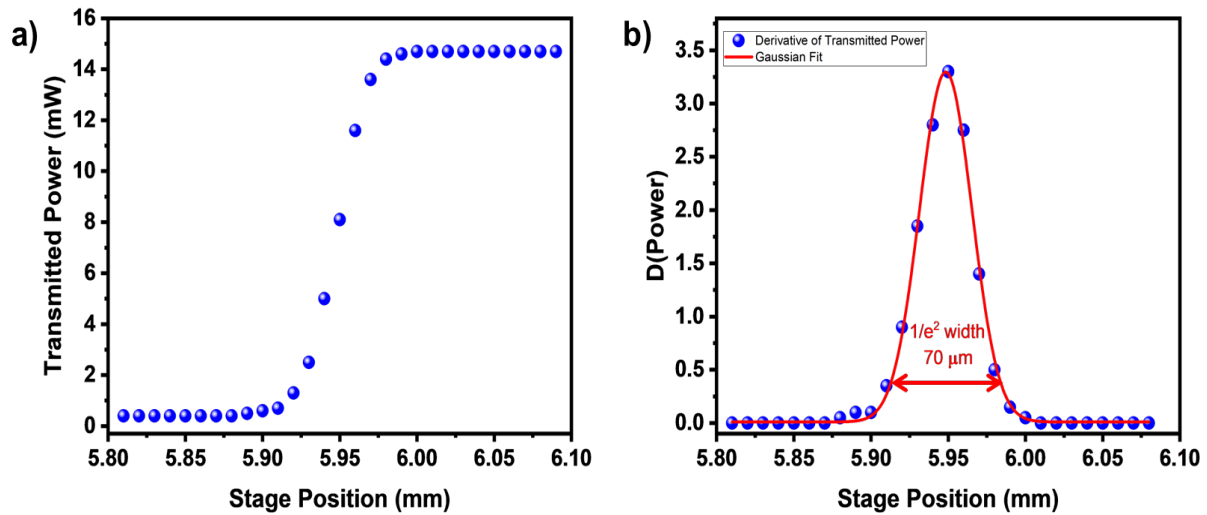


Figure 2.3. Beam Diameter at the Sample Position: (a) Transmitted power against knife-edge position. (b) Gaussian profile reconstructed by taking the derivative of transmitted power.

Considering the SHG beam to be generated from the area on the sample that is illuminated by the excitation beam, the $1/e^2$ diameter of the SHG beam at the sample will be $\sim 50\ \mu\text{m}$ (Appendix A3). The reflected beam from the sample was collimated by a 50 mm plano-convex lens, so the diameter of the collimated beam will be ~ 1.5 mm for the fundamental (excitation) beam, and ~ 1 mm for the second harmonic beam. The collimated beam was focused to the entrance slit of the spectrometer using a 200 mm plano-convex lens, so the diameter at the slit will be $\sim 290\ \mu\text{m}$ for the fundamental and $\sim 200\ \mu\text{m}$ for the second harmonic beams. The size of the slit was kept to be $380\ \mu\text{m}$ (0.015 inch).

Chapter 3

Results and Discussion

3.1 Characterization

3.1.1 Optical Microscopy and Raman Spectroscopy of Td-WTe₂

To understand the surface morphology of the Td-WTe₂ samples, we recorded the optical microscopic images of the Td-WTe₂ single crystal and Td-WTe₂/Si thin film (Figure 3.1a,b). It is evident that the thin film has formed as non-uniform patches on the substrate. The Raman spectrum from the pure single crystal and the thin film was obtained using a 532 nm laser excitation source.

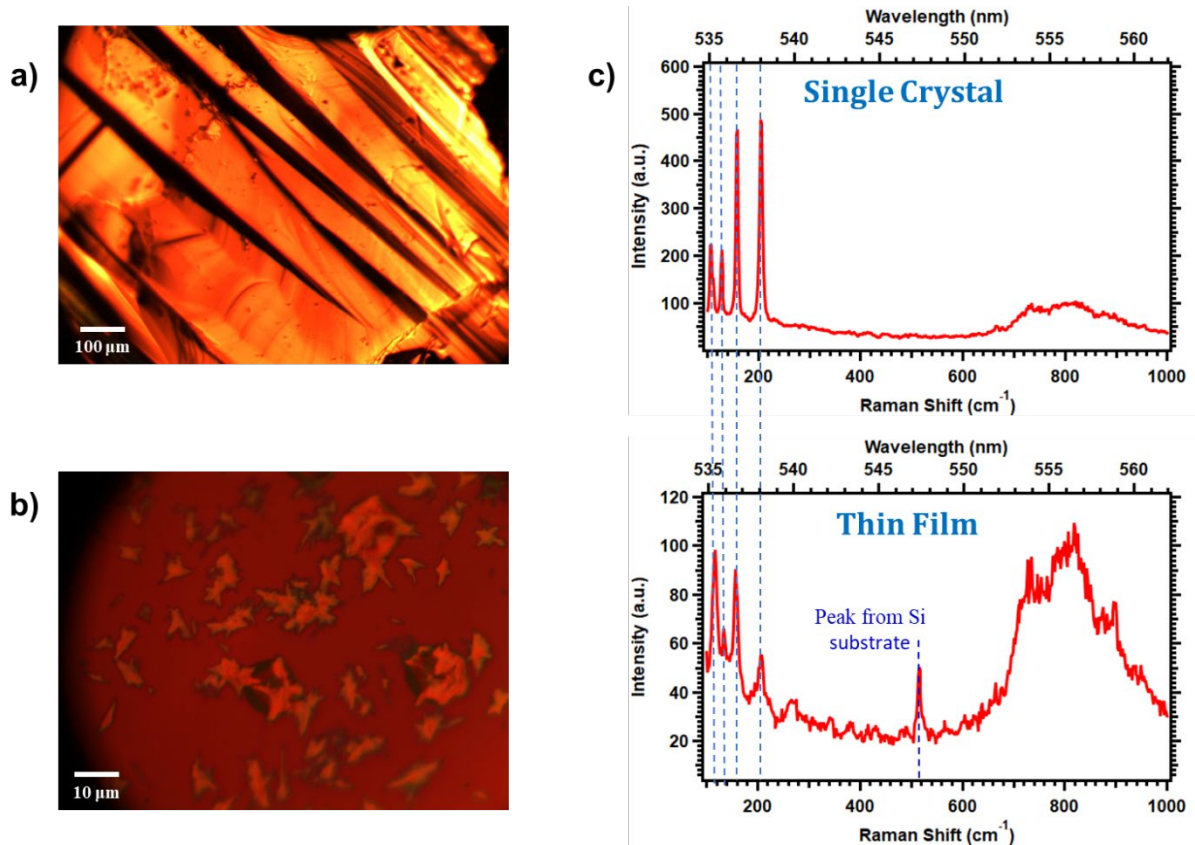


Figure 3.1. Optical Characterization of Td-WTe₂: Optical microscopic images of (a) Td-WTe₂ single crystal under 10X and (b) Td-WTe₂/Si thin film under 100X. c) Raman spectra of Td-WTe₂ single crystal and Td-WTe₂/Si thin film.

The characteristic phonon peaks³² from the thin film correspond well with that of the single crystal (Figure 3.1c), confirming that Td-WTe₂ has formed on the substrate. The thin film also has a peak from the Si substrate at 520 cm⁻¹.

3.1.2 Optical Characterization of Mn₃Sn/LaAlO₃ Thin Film

The optical images of Mn₃Sn/LaAlO₃ thin film also show a patchy texture (Figure 3.2). However, the poor contrast suggests that the patches are irregularities within the film surface, rather than the film itself being discrete discontinuous patches. We also observed electrical conductivity upon placing multimeter tips on two ends of the film, indicating that the film is probably continuous.

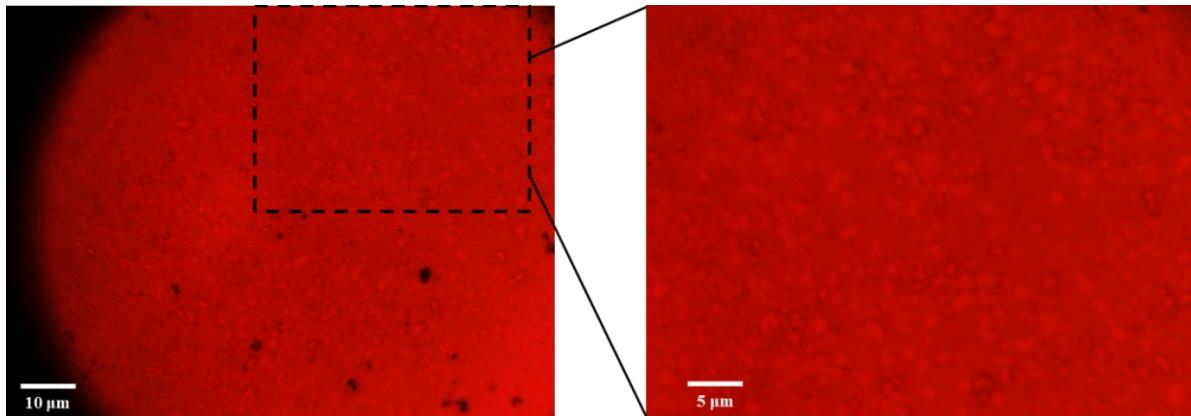


Figure 3.2. Optical Characterization of Mn₃Sn: The optical image of Mn₃Sn thin films on LaAlO₃ substrate under 100X microscope.

3.1.2 X-Ray diffraction spectrum of Mn₃Sn/LaAlO₃ Thin Film

To understand the crystal orientation, we recorded the XRD spectrum of the Mn₃Sn/LaAlO₃ thin film. Mn₃Sn crystallizes in a hexagonal P6₃/mmc space group.³³ The XRD spectrum of the Mn₃Sn/LaAlO₃ thin film shows only the Mn₃Sn (0002) and (0004) peaks (Figure 3.3a), indicating that the film is oriented in the (0001) direction (c-axis).³⁴ The approximate thickness of the film was estimated using the Scherrer equation:³⁵

$$\tau = \frac{0.93 \times \lambda}{\beta \times \cos(\theta)}$$

where τ is the crystallite thickness, λ is the X-ray wavelength, β is full width at half maximum (FWHM) of the Bragg diffraction peak in radian, and θ is the Bragg diffraction angle.

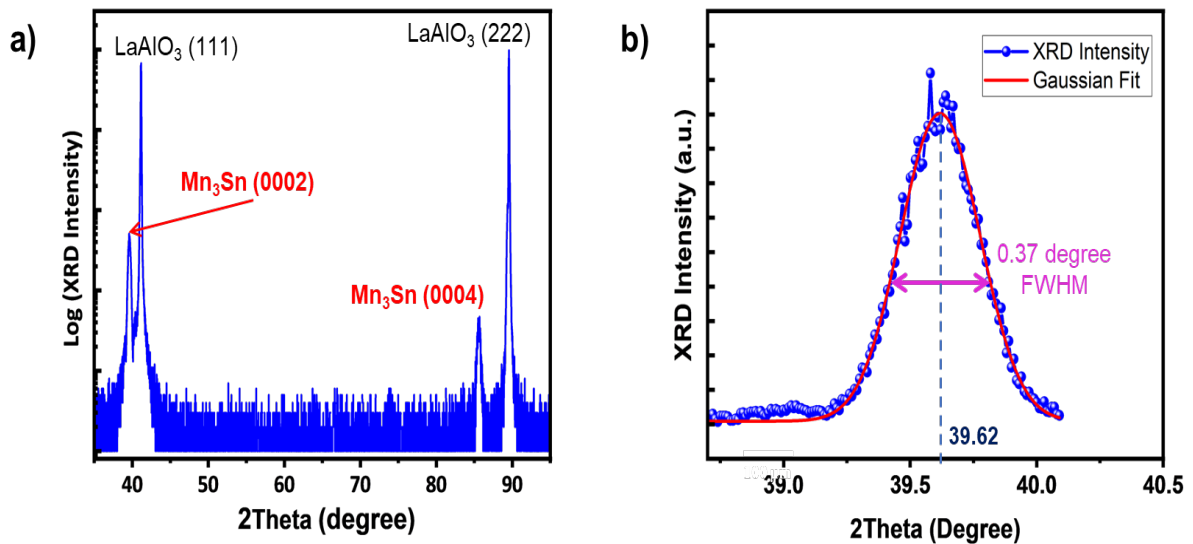


Figure 3.3. PXRD Spectra: a) The PXRD spectrum of Mn₃Sn on LaAlO₃ substrate. b) Gaussian fit of Mn₃Sn (0002) peak. The XRD spectrum was recorded by Mr. Prajwal Laxmeesha, from May group at Drexel University.

By using $\lambda = 0.15406$ nm (Cu-K α), and $\beta = 0.00646$ radian (0.37 degree), $\theta = 0.34575$ radian ($39.62/2 = 19.81$ degree) from the Mn₃Sn (0002) peak (Figure 3.3b), we get the thickness to be ≈ 22 nm.

3.1.3 AFM Image of Td-WTe₂/Si Thin Film

To determine the thickness of the Td-WTe₂ thin film, we recorded the AFM image (Figure 3.4a). The line profile shows an average thickness of 3-5 nm, corresponding to 4-7 layers of Td-WTe₂ (interlayer spacing in WTe₂ is 0.75 nm³⁶).

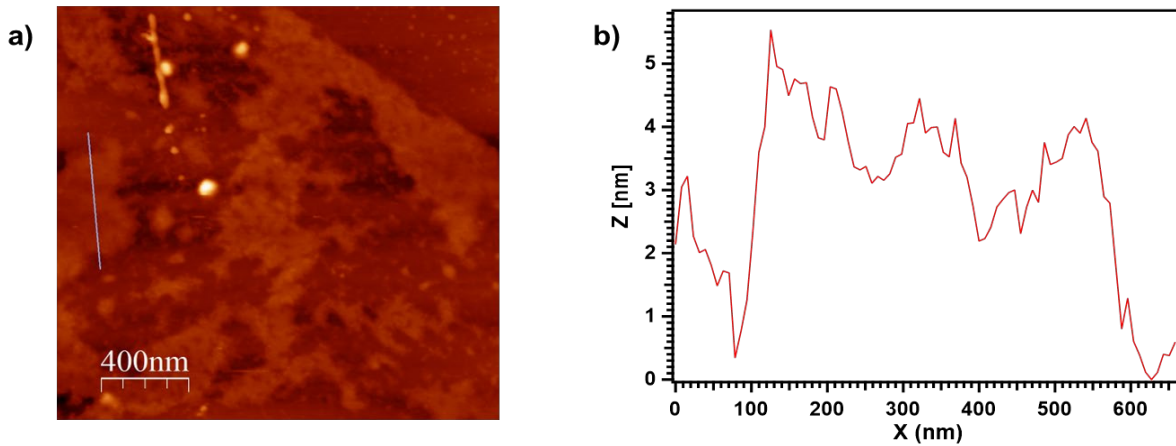


Figure 3.4. AFM Image of Td-WTe₂/Si Thin Film: The (a) AFM image and (b) thickness profile showing an average thickness of 3-5 nm for the film. The AFM image was recorded by Ms. Uddipana Kakati, from Strongin group at Temple University.

3.1.4 STM Image of Td-WTe₂ Single Crystal

To understand the fine surface morphology of the Td-WTe₂ single crystal, we recorded the STM image. The STM image (Figure 3.5) on an area of 200x200 nm shows that the surface is a little rough, with a height difference up to 1.5 nm (corresponding to 2 layers) within a scan length of 55 nm.

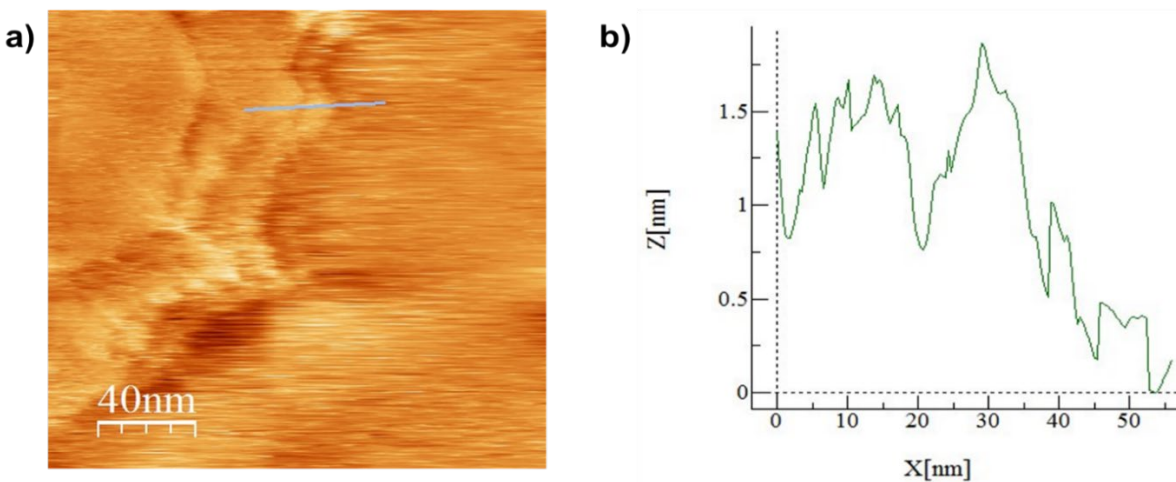


Figure 3.5. STM Image of Td-WTe₂ Single Crystal: (a) The STM image of Td-WTe₂ single crystal. (b) Line profile showing the variation in surface. The STM images were recorded by Mr. Amuthan Dekshinamoorthy from the Borguet group.

3.2 Wavelength and Polarization Dependent SHG from WTe₂ and Mn₃Sn

To understand the impact of the material properties and band structure on the SHG response of the topological Weyl semimetals, we conducted wavelength dependent SHG studies on Td-WTe₂/Si and Mn₃Sn/LaAlO₃ thin films. Since the Weyl semimetals do not have a bandgap, it is necessary to look for other electronic features to understand the effect of the band structure on the SHG response. A theoretical study by Abdollahipour and coworkers³⁷ predicted surface plasmon polariton (SPP) modes in Weyl semimetals in the NIR regime. Since SPPs involve polarization of the electron cloud, we hypothesize to observe an enhancement for SHG at SPP resonant wavelengths. Hence, we performed wavelength dependent SHG studies on Td-WTe₂/Si and Mn₃Sn/LaAlO₃ thin films in the NIR regime.

The SHG experiments were conducted in the NIR idler output range of our OPA, ORPHEUS-HP (refer to Section 2.6 for details), varying the wavelength from 1200-1800 nm in steps of 10 nm. The output of our laser is vertically polarized, which would correspond to s-polarization for the vertically mounted sample. Since p-polarized light provides a higher coupling with surface plasmon modes than s-polarized light³⁸, we used a periscope to rotate the polarization of the pump beam to horizontal so that the sample experiences a p-polarized excitation. The incident angle was kept at 60°. The experiments were conducted at a constant laser repetition rate of 25 kHz, and a variable density N.D. filter was used to keep a constant power of 10 mW for all the wavelengths. The beam diameter was measured to be 70 μm at the sample (Section 2.6), and taking into account the elliptical area illuminated (Figure 3.6),

$$\begin{aligned} \text{Area illuminated} &= \pi \times a \times b \\ &= \pi \times 70 \times \frac{70}{\cos(60)} \mu\text{m}^2 = 3.08 \times 10^4 \mu\text{m}^2 \\ &= 3.08 \times 10^{-4} \text{cm}^2 \end{aligned}$$

$$\text{Energy per pulse} = \frac{\text{Average Power}}{\text{Repetition rate}}$$

$$= \frac{10 \times 10^{-3} \text{ W}}{25 \times 10^3 \text{ Hz}} = 0.4 \mu\text{J}$$

$$\therefore \text{Fluence} = \frac{\text{Energy per pulse}}{\text{Effective spot area}}$$

$$\begin{aligned}
&= \frac{0.4 \times 10^{-6} J}{3.08 \times 10^{-4} \text{ cm}^2} \\
&= 1.3 \text{ mJ/cm}^2
\end{aligned}$$

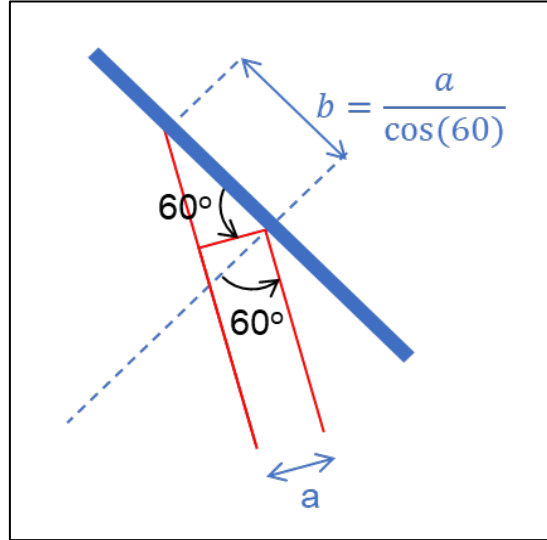


Figure 3.6. Schematic of area illuminated: Out of plane beam spot size remains “a”, while in plane beam spot size = $a/\cos(60)$. Therefore, area illuminated = $\pi \times a \times a/\cos(60)$.

We used an s-p polarizer after the sample to perform the experiment in the PP (p-excitation, collection of p-SHG) and SP (p-excitation, collection of s-SHG) polarization combination geometries. The measurements were done by integrating for 5-20 seconds depending on the signal strength, and all spectra were scaled down to 1s for comparison.

3.2.1 SHG in PP Geometry

The SHG response of Td-WTe₂/Si (Figure 3.7a) in the PP geometry was recorded by integrating for 5s, and scaled down to 1s. The wavelength dependent spectra show a considerable interference type of behaviour (Figure 3.7b). It is possible that the output from the front and back surface of the WTe₂ film can interfere, considering the film is less than 5 nm thick, as well as the front and back reflection from the silicon substrate.

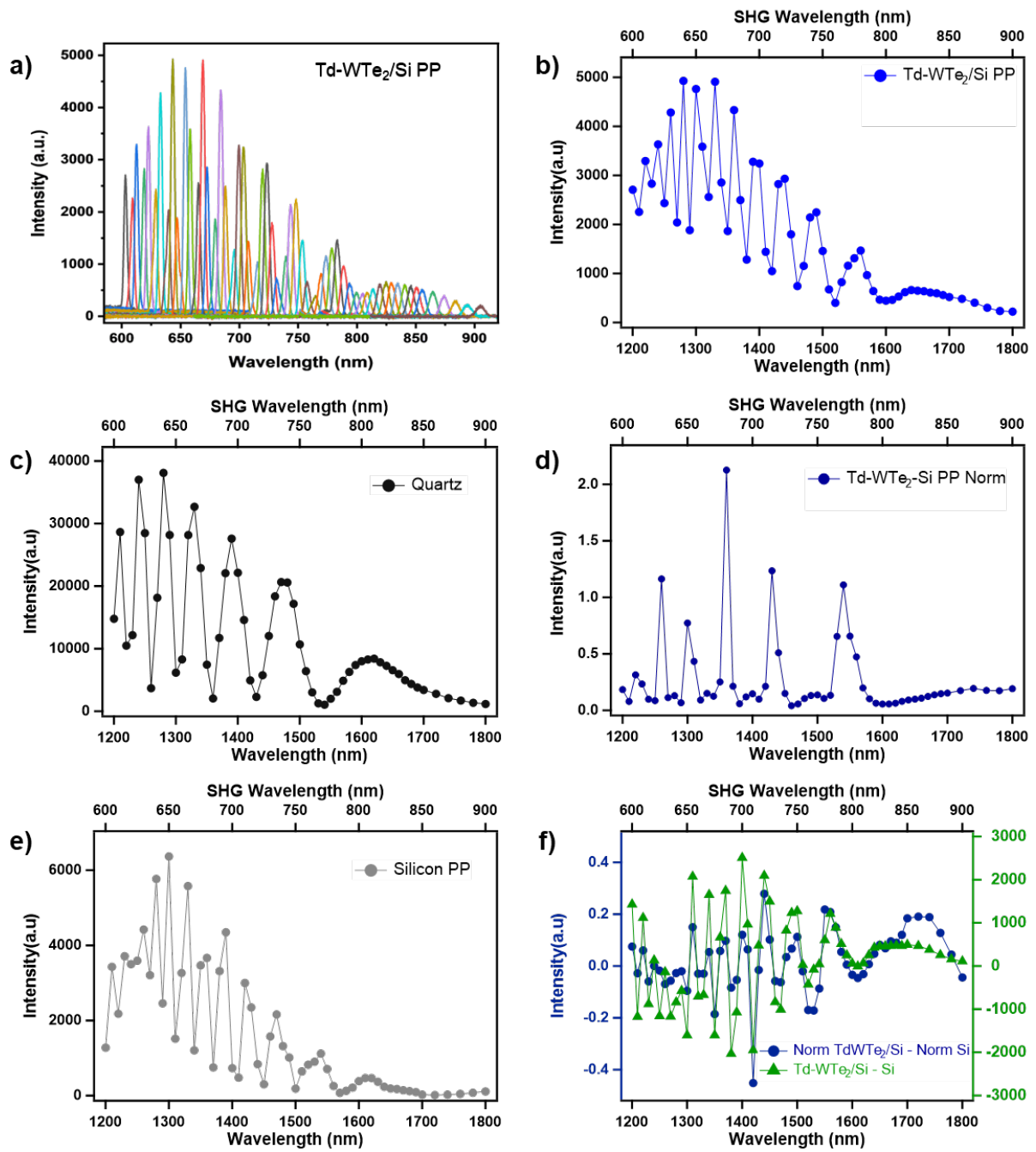


Figure 3.7. SHG PP Response of Td-WTe₂/Si: (a), (b) Wavelength-dependent SHG output of Td-WTe₂/Si in the PP geometry. (c) Total SHG response of Quartz. (d) PP-SHG response of Td-WTe₂/Si normalized with the SHG response of quartz. (e) PP-SHG response of Si substrate. (f) Si-response corrected PP-SHG spectrum of Td-WTe₂.

To take into account the instrumental characteristics like the efficiency of the grating and detector (see Appendix A4), change in focusing with wavelength, etc., we used the SHG response from a z-cut α -quartz, which is a commonly used as a standard reference for wavelength and phase dependent NLO experiments.³⁹⁻⁴⁰ However, the quartz spectrum also shows an interference pattern (Figure 3.7c), probably from the front and back surface of quartz. The interference pattern persists in the Td-WTe₂/Si PP-SHG spectrum normalized with quartz (Figure 3.7d), as the interference pattern is highly dependent on the path difference between the interfering signals, and we don't have a complete control on the thickness of the sample and the reference. We do not observe any characteristic features in the normalized PP-SHG spectrum of Td-WTe₂/Si thin film. To remove the contributions from the Si substrate, we also recorded the wavelength dependent PP-SHG spectrum of a neat Si substrate of approximately same thickness as that of the substrate in Td-WTe₂/Si thin film (~0.3 mm). The interference pattern is present in the PP-SHG spectrum of Si as well (Figure 3.7e). The raw and normalized spectra of Td-WTe₂/Si thin film were corrected using raw and normalized PP-SHG spectrum of Si respectively (Figure 3.7f), and the relative magnitude of the signal with respect to that of the oscillations due to the interference make it difficult to comment on the wavelength-dependent behaviour of the PP-SHG in Td-WTe₂/Si thin film.

We also recorded the wavelength dependent PP-SHG response of Mn₃Sn/LaAlO₃ thin film (Figure 3.8a), integrating for 5s and then scaled down to 1s. The interference behaviour is present in the wavelength dependent spectrum of Mn₃Sn/LaAlO₃ thin film as well (Figure 3.8b), and as in the case of Td-WTe₂/Si thin film, after normalization with SHG spectrum of quartz (Figure 3.8c), the interference persists (Figure 3.8d). Interestingly, the interference pattern is not present in the PP-SHG spectrum of the neat LaAlO₃ substrate (Figure 3.8e). But it is still difficult to make any comment on the wavelength-dependent PP-SHG spectra of Mn₃Sn/LaAlO₃ due to the relative magnitude of the signal and the interference.

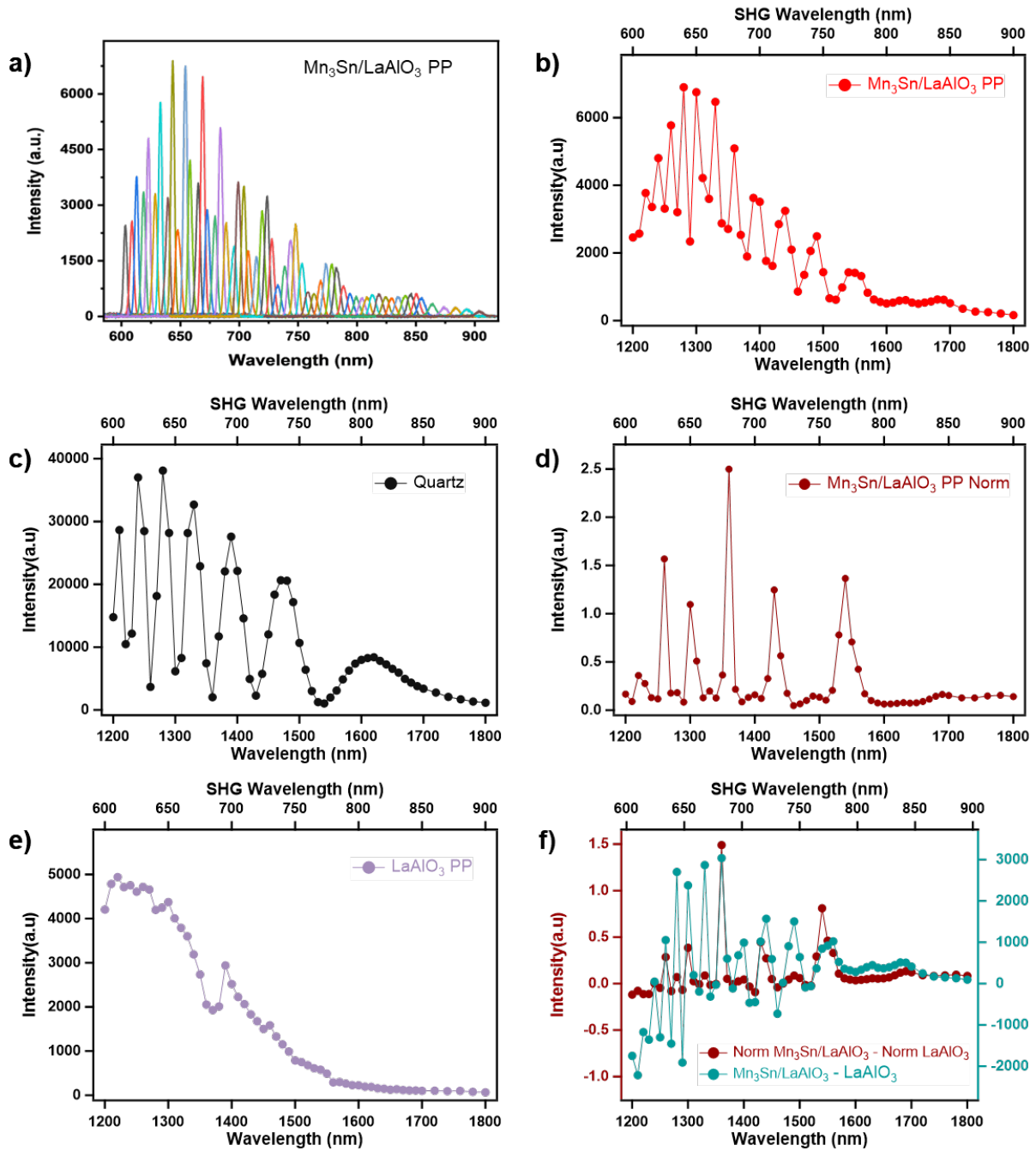


Figure 3.8. PP-SHG Response of Td-WTe₂/Si and Mn₃Sn/LaAlO₃ thin films: (a), (b) Wavelength-dependent SHG output of Mn₃Sn/LaAlO₃ in the PP geometry. (c) Total SHG response of Quartz. (d) PP-SHG response of Mn₃Sn/LaAlO₃ normalized with the SHG response of quartz. (e) PP-SHG response of LaAlO₃ substrate. (f) LaAlO₃ - response corrected PP-SHG spectrum of Mn₃Sn.

3.2.2 SHG in SP Geometry

Since we are exciting the samples with p-polarized light, ideally the SHG response should also be p-polarized. However, we observe that there is a significant response, almost 10% of the PP intensity for both Td-WTe₂/Si and Mn₃Sn/LaAlO₃ in the SP polarization geometry (Figure 3.9a-d). This must be due to the uneven nature of the surface of the thin films, which can change the polarization of the reflected light, resulting in sufficient amount of s-polarization in the reflected fundamental and second harmonic beams. The SP-SHG spectra also show relatively much less interference behaviour compared to the PP-SHG spectra.

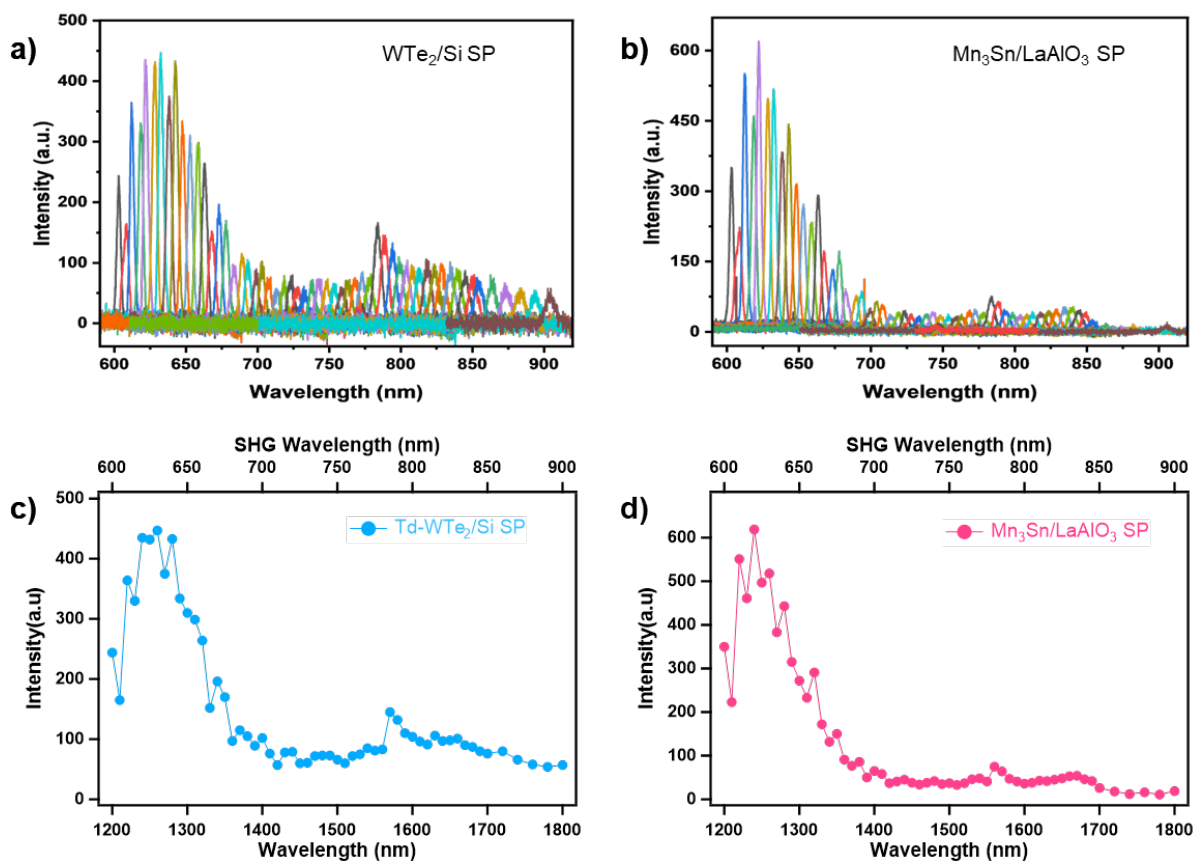


Figure 3.9. PP-SHG Response of Td-WTe₂/Si and Mn₃Sn/LaAlO₃ thin films: Wavelength-dependent PP-SHG response of Td-WTe₂/Si (a,c) and Mn₃Sn/LaAlO₃ (b,d) thin films, and the PP-SHG spectra normalized with quartz of (e) Td-WTe₂/Si and (f) Mn₃Sn/LaAlO₃ thin films.

Some amounts of oscillations are present in the SP-SHG spectra normalized with quartz of Td-WTe₂/Si (Figure 3.10a) and Mn₃Sn/LaAlO₃ (Figure 3.10b), evidently due to the interference present in the spectrum of quartz. Therefore, it is important to figure out how to improve our experimental conditions to get rid of the interference behaviour.

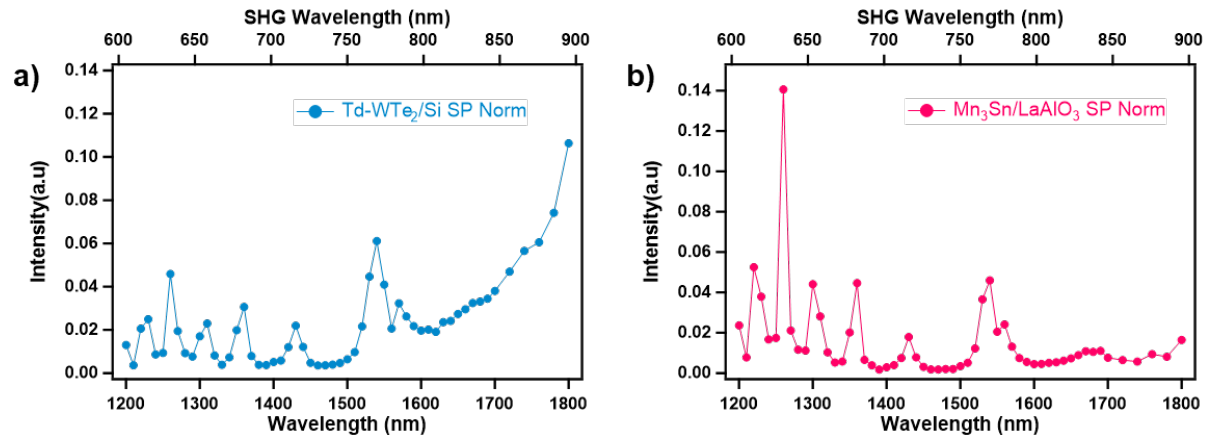


Figure 3.10. Normalized SP-SHG Spectra of Td-WTe₂/Si & Mn₃Sn/LaAlO₃ thin films: SP-SHG spectra of (a) Td-WTe₂/Si and (b) Mn₃Sn/LaAlO₃ normalized with SHG spectrum of Quartz.

An interesting observation is that in the normalized SP-SHG spectrum of Td-WTe₂/Si is that the intensity starts increasing beyond 1600 nm, which is not observed in the spectrum of Mn₃Sn/LaAlO₃. A study by Meng and coworkers⁴¹ has shown an enhancement in transitions near the Weyl point of Td-WTe₂, in the energy range 0.5-0.8 eV (2500-1550 nm). We expect the enhancement in our spectrum to be due to this. However, we need to do further experiments before we can make any reasonable claims.

The neat substrates showed a negligible SP-SHG output, as expected because of their uniform flat surface. We were able to record the SP-SHG intensity of Si recorded at 1300 nm after integrating for 120 s, which is nearly 4 orders of magnitude lower than it's PP-SHG intensity (Figure 3.11).

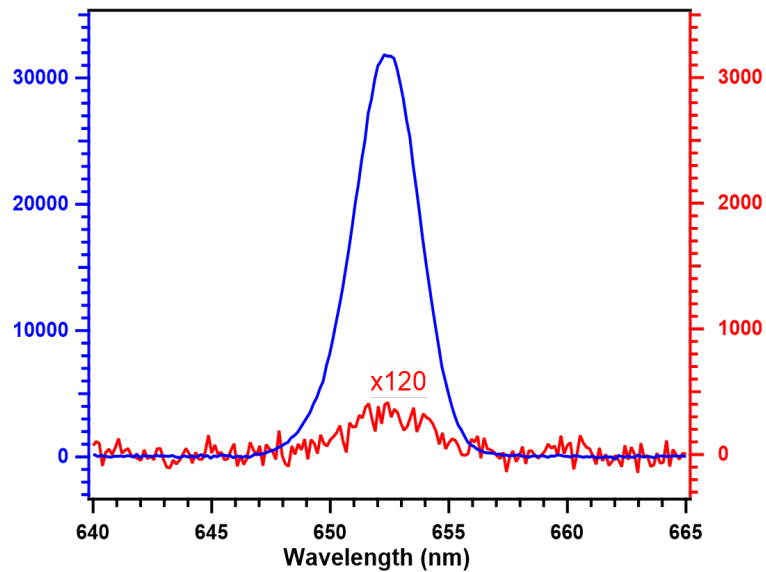


Figure 3.11. Comparison of SP and PP SHG Intensity of Si: The comparison of SP-SHG intensity of Si at 1300 nm is nearly 4 orders of magnitude lower than it's PP-SHG intensity.

3.3 SHG from Td-WTe₂ Single Crystal

We also performed reflection SHG measurements from the Td-WTe₂ single crystal. However, the reflection from the single crystal is highly scattered and distorted, probably due to the high unevenness of the crystal surface (see optical image, Figure 3.1a). We recorded the SHG output from the single crystal at 1300 nm after sufficient optimization and alignment of the experimental setup, and the response from the single crystal is ~5 times smaller than that of the Td-WTe₂/Si thin film (Figure 3.12). We need to optimize the experimental setup further to perform a wavelength dependent study on the Td-WTe₂ single crystals.

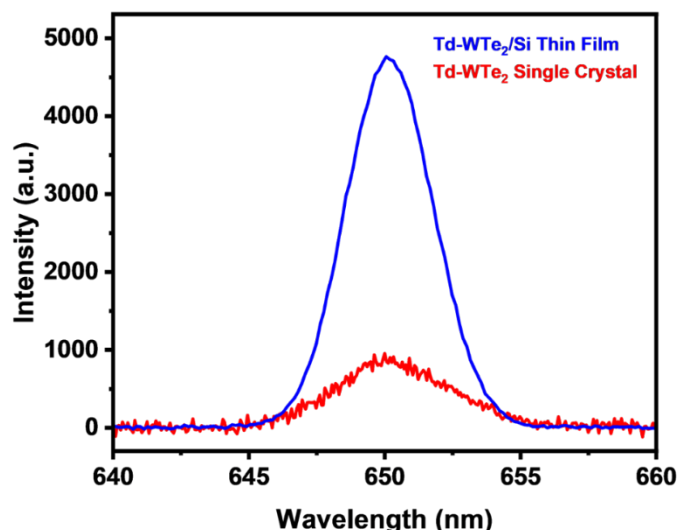


Figure 3.12. SHG From Td-WTe₂ Single Crystal: The SHG response from Td-WTe₂ single crystal is ~5 times smaller than that from Td-WTe₂/Si thin film, likely due to highly uneven nature of the surface.

3.4 Stability During SHG Experiments

The SHG is an NLO process, and therefore there are chances of undesirable changes occurring to the system during the high intensity irradiation like structural deformation, charge build up, etc.⁴²⁻⁴³ To have any meaningful understanding of the system, it is important that the samples remain stable during the SHG experiments. So, we performed a few experiments to study the stability of the samples during the SHG experiments.

3.4.1 Power Dependence of SHG

The SHG intensity should vary as the square of excitation beam intensity (refer to equation 1.2). We observe that both Td-WTe₂/Si (Figure 3.13a) and Mn₃Sn/LaAlO₃ (Figure 3.13b) thin films show a quadratic increase of SHG intensity with increase in excitation beam intensity from 2 mW to 14 mW at 25 kHz repetition rate.

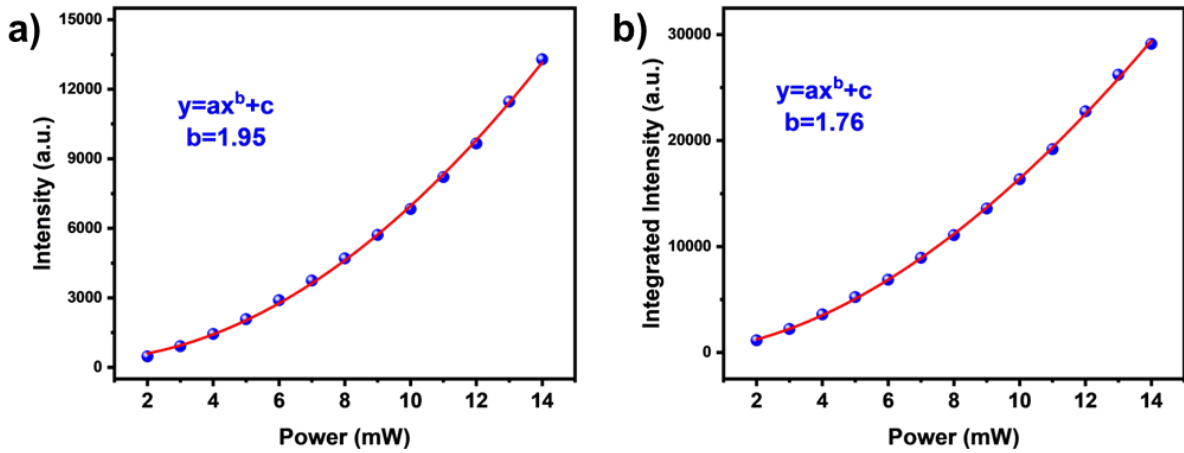


Figure 3.13. Power Dependence of SHG: Excitation power-dependent SHG intensity of (a) Td-WTe₂/Si and (b) Mn₃Sn/LaAlO₃ thin films showing a quadratic dependence up to 14 mW.

3.4.2 SHG Output vs Time

To check if continuous laser illumination affects the SHG response of the materials, we irradiated the WTe₂ and Mn₃Sn thin films with 1310 nm light at 14 mW power continuously for 30 minutes, and recorded the SHG output every 5 minutes (Figure 3.14). We observed that the SHG output remains pretty stable during the entire duration, indicating that the samples do not undergo any considerable changes during the process.

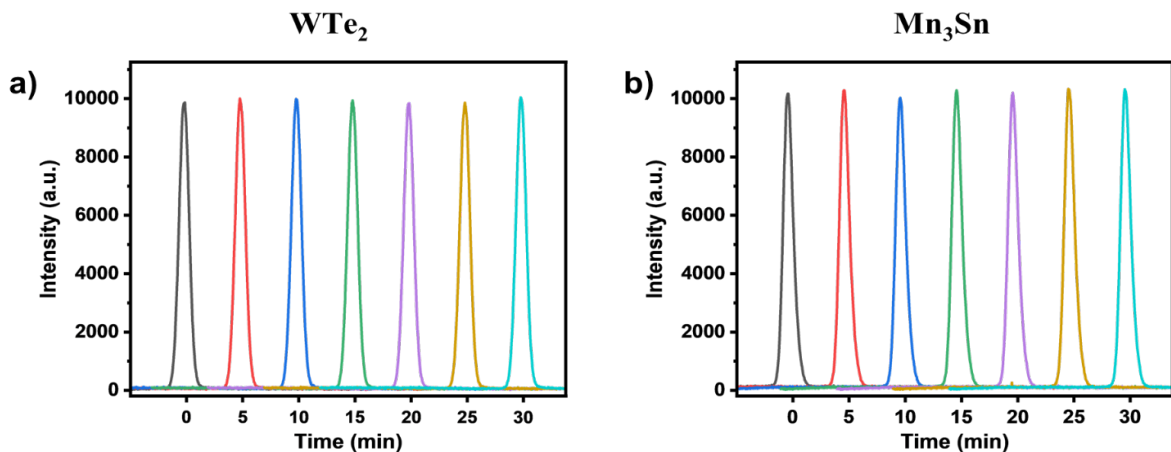


Figure 3.14. SHG vs Time: The SHG output of (a) Td-WTe₂/Si and (b) Mn₃Sn/LaAlO₃ thin films over 30 minutes of continuous laser irradiation.

3.4.3 SHG Dependence on Laser Repetition Rate

The repetition rate of the laser determines the number of pulses hitting the sample per second. If any heating or charging effects come into play during the SHG process, the heat/charge should start accumulating in the system if we increase the laser repetition rate, and thereby affect the SHG response. So, to check if any heating or charging effects come into play during the SHG process, we collected the SHG response as function of laser repetition rate from $\text{Mn}_3\text{Sn}/\text{LaAlO}_3$ thin film, varying the repetition rate from 10 kHz to 150 kHz. The energy per pulse remains constant at all the repetition rates, so the intensity experienced by the sample remains the same (Figure 3.15a). But the increased number of pulses will result in linear increase in power (Figure 3.15b). So, the SHG output should increase linearly with increase in the laser repetition rate.

The SHG intensity of $\text{Mn}_3\text{Sn}/\text{LaAlO}_3$ thin film at 1280 nm was recorded while increasing the laser repetition rate from 10 kHz to 150 kHz, and back to 10 kHz. The SHG intensity varies linearly with the laser repetition rate, with very little hysteresis between the forward and backward scans (Figure 3.15c). The linear fit to the log-log plot of the SHG intensity and laser repetition rate also gives a slope of ~ 1 (Figure 3.15d). So, we are able to confirm that there isn't any considerable heat build-up or charging effects happening in the $\text{Mn}_3\text{Sn}/\text{LaAlO}_3$ thin film up to 150 kHz.

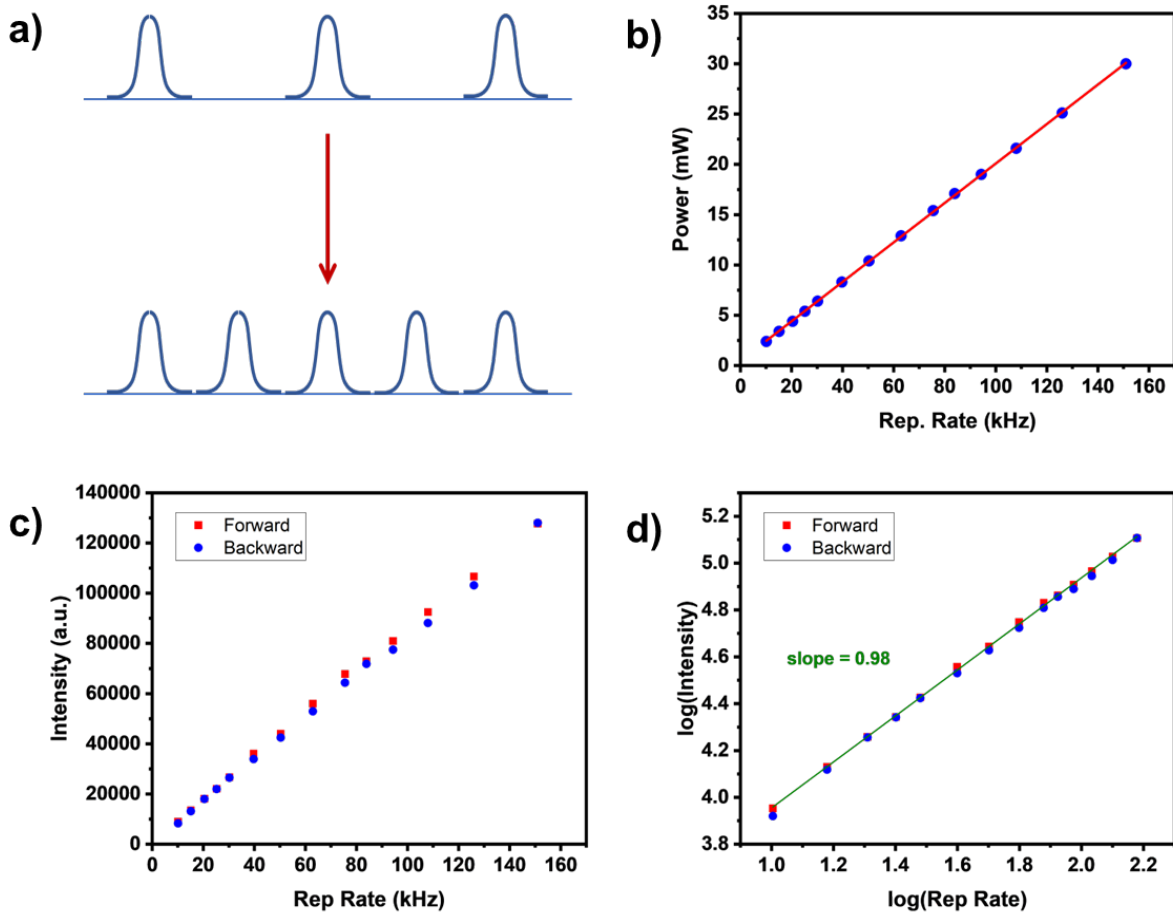


Figure 3.15. Dependence of SHG Output on Laser Repetition Rate: (a) Schematic of varying the laser repetition rate. (b) Linear increase in laser output power with increase in repetition rate. (c) SHG intensity vs laser repetition rate for $\text{Mn}_3\text{Sn}/\text{LaAlO}_3$ thin film, showing a linear increase, a very little hysteresis between forward and backward scans. (d) Linear fit to log-log plot of SHG intensity and laser repetition rate giving a slope ~ 1 .

Chapter 4

Thesis Summary and Future Outlook

In this thesis, we used reflection surface SHG spectroscopy to study the surfaces of topological Weyl semimetals Td-WTe₂/Si and Mn₃Sn/LaAlO₃ thin films by varying the wavelength from 1200-1800 nm in the PP and SP polarization geometries, with the aim of identifying some topological signatures. We observe that by using the appropriate polarization geometry, we can extract information from uneven thin film surfaces selectively without the contribution from the substrates, with the SP-SHG spectra from Td-WTe₂/Si and Mn₃Sn/LaAlO₃ thin films having negligible contribution from the substrates. We observe an increase in the SP-SHG intensity of Td-WTe₂/Si thin film above 1600 nm, suggesting some sort of enhanced transitions in this region for Td-WTe₂. Some interference effects come into play due to the responses from different surfaces, both from the sample and the substrate, as well the reference, affecting the analysis of the SHG response of the samples. The Td-WTe₂/Si and Mn₃Sn/LaAlO₃ thin films do not show any heating or charging effects during our experiments upon with increase in the intensity of the laser and laser repetition rate, or with continuous laser irradiation.

We need to perform further experiments in a broader wavelength range to have an understanding of the effect of topological states on the SHG response of these Weyl semimetal samples. The first challenge to be addressed is to remove the interference patterns from the SHG spectra. Varying the angle of incidence and the polarization of the excitation beam has to be tried out to see if these parameters have an effect on the interference. The SP-SHG spectrum of Td-WTe₂/Si thin film has to be recorded for wavelengths longer than 1800 nm to have an understanding of the enhancement beyond 1600 nm, keeping in mind the efficiency of the detection and other instrumental parameters. As a resonance in both the fundamental as well as the second harmonic wavelength can give a resonance in SHG, sum frequency generation, which is also a second order NLO process, can be performed to identify the exact energy of the resonance. Time-resolved SHG measurements can give an idea about the band geometry and carrier dynamics responsible for the enhancement. Since the Weyl points have a definite chirality, excitation polarization dependent measurements with

linear and circularly polarized light can give further insights about the topological states. We can also employ functionalizing of the surfaces via chemical modifications to see how the surface band properties are affected. An extensive study by varying these different parameters can help to get a broad and fundamental understanding of the topological Weyl semimetals, and thereby further improve their potential in a wide variety of applications.

Appendix

A1. Studying the Stability During Electrochemical Activity

As discussed in the introduction, Weyl semimetals have potential applications as electrochemical catalysts. To understand if catalytic activities affect the stability and properties of Td-WTe₂, we recorded the Raman spectrum from a Td-WTe₂ single crystal which was used for electrochemical reduction of CO₂ by the Strongin group, Temple University. The electrochemical experiments were performed by Benjamin Roe, from Strongin group at Temple University, using a Td-WTe₂ single crystal as working electrode in acetonitrile solvent with 0.2M 1-ethyl-3-methylimidazolium tetrafluoroborate (EMIMBF₄) ionic liquid as the electrolyte.

The comparison between the spectra of the pure Td-WTe₂ and the single crystal after electrochemistry (Figure A1.1a) shows that the characteristic phonon peaks remain intact after the electrochemical activity. However, a small hump appears in the longer wavenumber region. We therefore performed the measurements in a longer range, and a number of peaks appeared in the single crystal used for electrochemistry (Figure A1.1b). So, we recorded the Raman spectrum of the ionic liquid EMIMBF₄ that was used in the electrochemical experiment, as some amount of the liquid might be trapped or intercalated in the sample. We observe that the extra peaks appearing in the single crystal match with the peaks of EMIMBF₄ (Figure A1.1c). This confirms that the Td-WTe₂ does not undergo any chemical change detectable with Raman measurements during the electrochemical process.

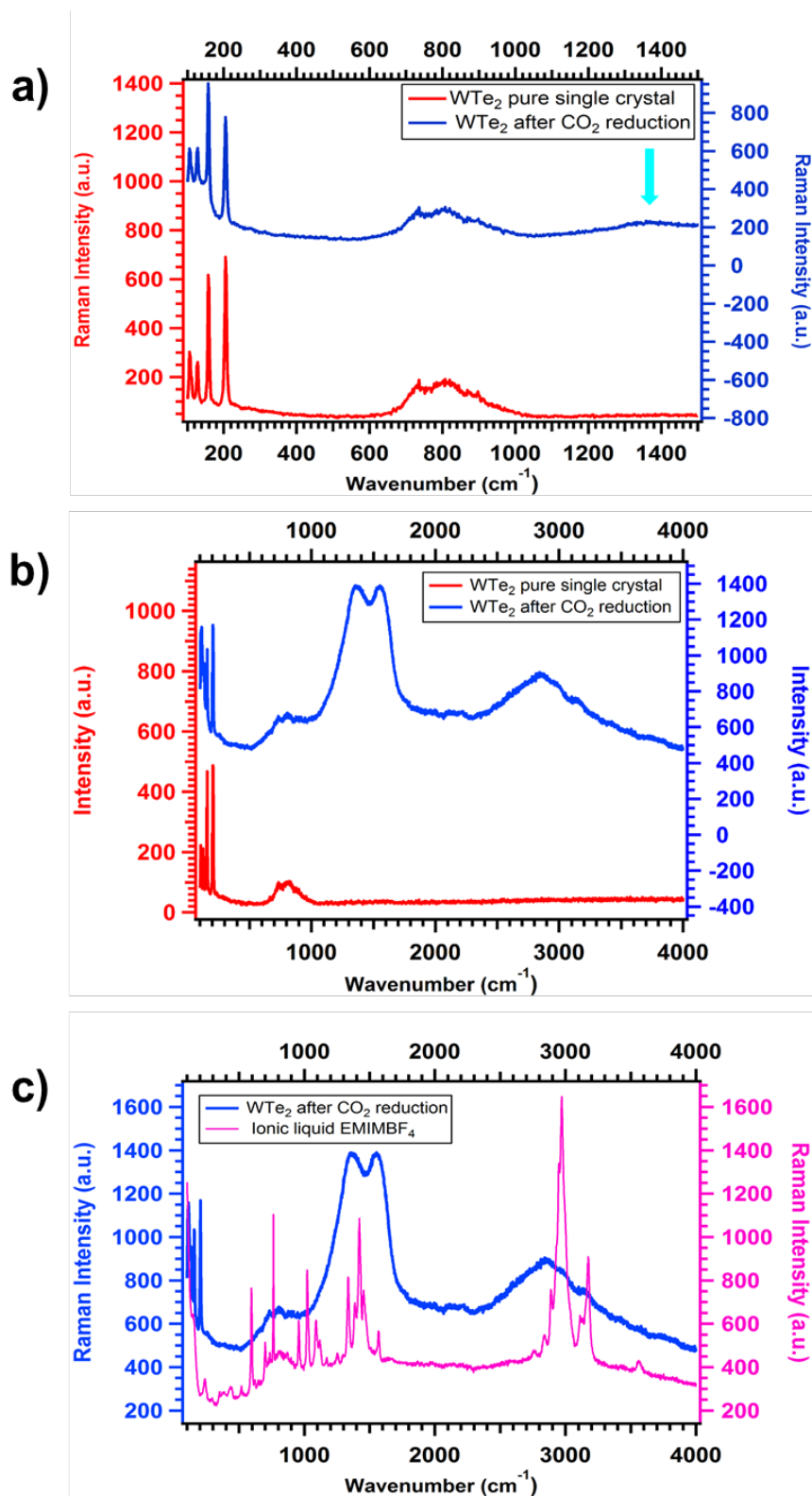
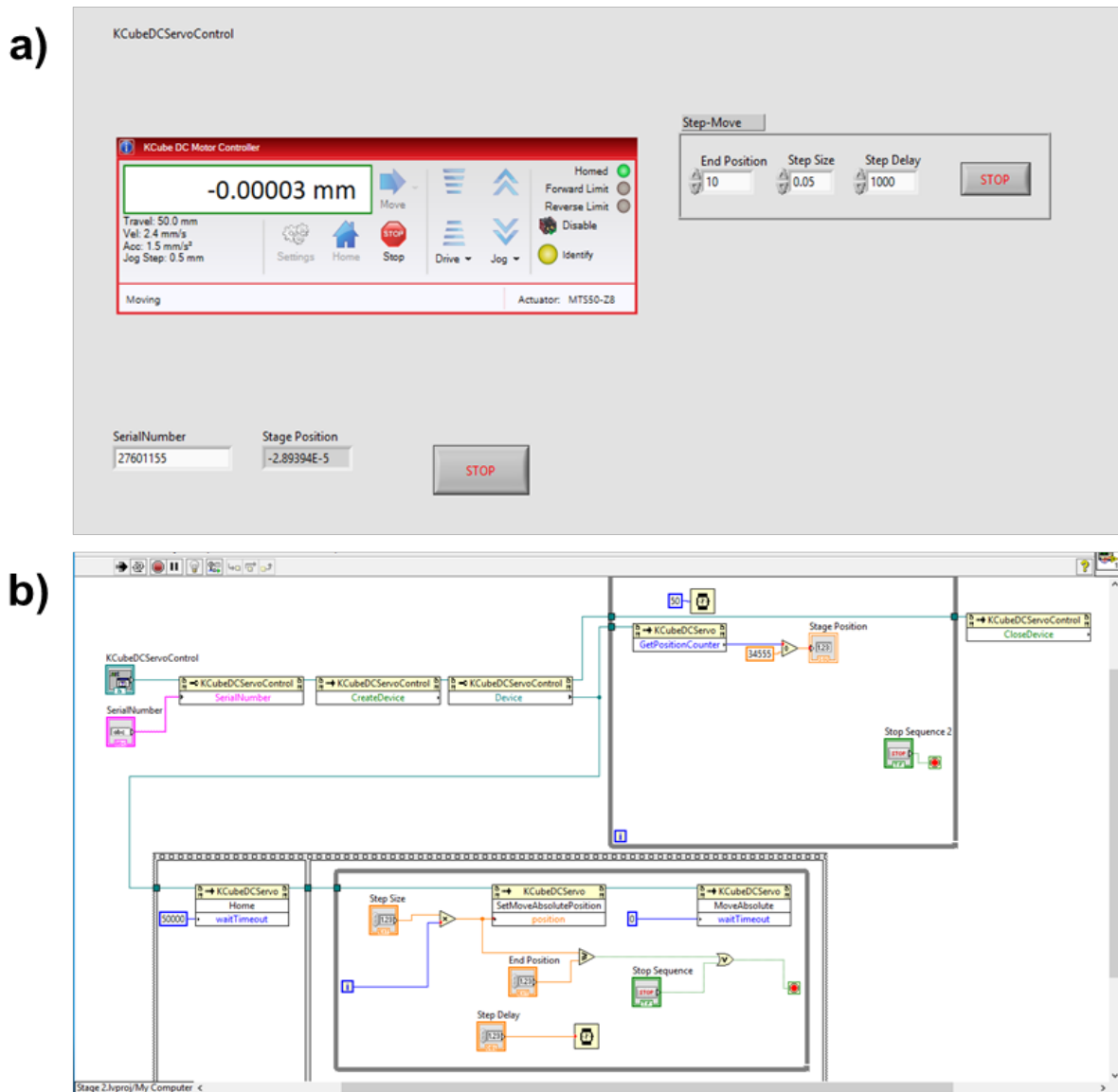


Figure A1.1. Raman Spectra after Electrochemical Activity: (a) Raman spectra of as-made and electrochemically cycled Td-WTe₂ single crystals. (b) Spectrum of electrochemistry performed Td-WTe₂ for an extended range (100-4000 cm⁻¹). (c) Spectrum of Td-WTe₂ and the ionic liquid EMIMBF₄ used for electrochemical CO₂ reduction.

A2. Automation of Delay Stage via LabVIEW

A LabVIEW program was developed to automate the delay stage for time-resolved experiments in the future (Figure A2.1). The program communicates to the Thorlabs MTS50-Z8 translation stage through a Kinesis interface via K-Cube DC Servo Motor Controller. The program can command the stage to move to specified positions, and to move at specified steps at discrete time intervals and adjustable velocities.



A3. Calculation of Beam Diameters

The beam diameter was measured using the knife-edge technique (Figure A3.1).³⁰ A knife-edge (razor blade) placed on a translation stage is moved along the cross section of the beam, and the transmitted laser power beyond the knife-edge is recorded as a function of the position of the knife-edge, as the beam is being blocked. The recorded power is the total integrated power of the Gaussian beam along its cross section, so the derivative of the transmitted power will give the Gaussian beam.

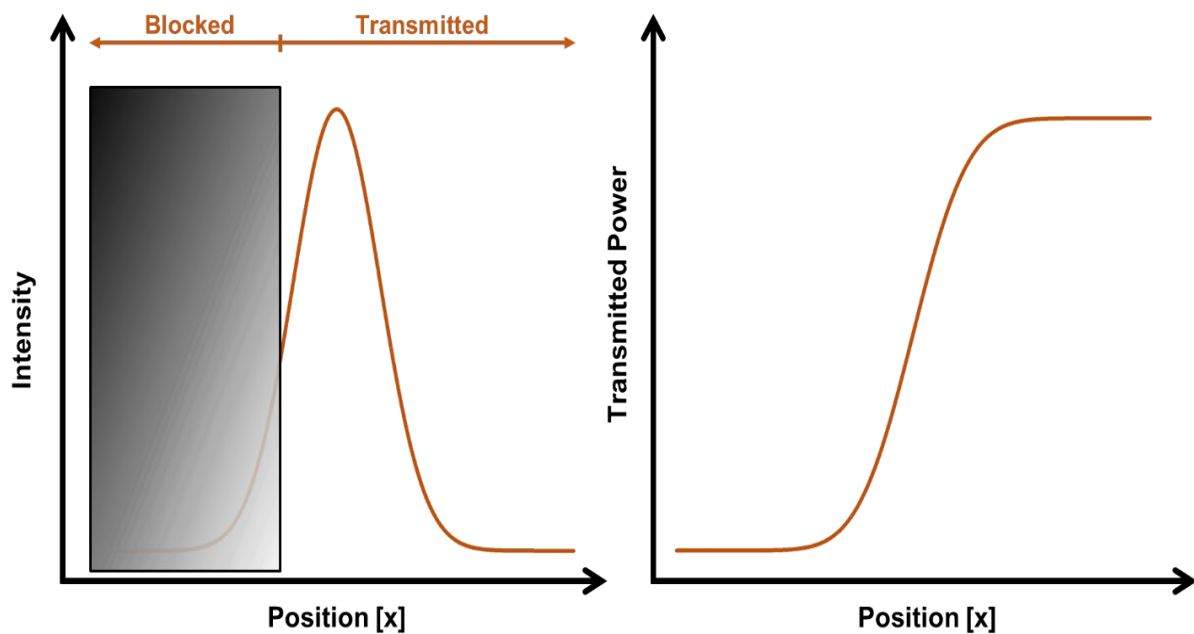


Figure A3.1. Knife-Edge Technique: The knife-edge is moved along the cross section of the beam, and the transmitted power is the integrated intensity over $[x]$.

The $1/e^2$ diameter of the laser beam before the 150 mm focusing lens in the SHG experimental setup is obtained to be 4.6 mm at 1200 nm. So, the theoretical diameter at the focal point will be (equation 2.1):

$$\begin{aligned}
 2w_0 &= \left(\frac{4M^2\lambda}{\pi} \right) \times \left(\frac{F}{D} \right) \\
 &= \left(\frac{4 \times 1 \times 1200 \times 10^{-6}}{\pi} \right) \times \left(\frac{150}{4.6} \right) \text{ mm} \\
 &= 50 \mu\text{m}
 \end{aligned}$$

The $1/e^2$ diameter of the beam at the focal point was measured to be $70 \mu\text{m}$. So, the M^2 of the beam will be:

$$M^2 = \frac{2w_0(\text{experimental})}{2w_0(\text{theoretical})} = \frac{70}{50} = 1.4$$

The equation of a Gaussian beam can be written as:

$$I = I_0 \exp\left(\frac{-(x - x_0)^2}{w_0^2}\right)$$

The SHG intensity is proportional to the square of the intensity of the excitation beam (equation 1.3). Therefore, SHG intensity,

$$I_{2\omega} \propto I_0^2 \exp\left(\frac{-2(x - x_0)^2}{w_0^2}\right)$$

$$i. e., = I_{2\omega} \propto I_0^2 \exp\left(\frac{-(x - x_0)^2}{\left(\frac{w_0}{\sqrt{2}}\right)^2}\right)$$

$$\therefore w_{SHG} = \frac{w_0}{\sqrt{2}} = \frac{70 \mu\text{m}}{\sqrt{2}} \approx 50 \mu\text{m}$$

So, by using equation 2.1 again, we can solve for D to get the diameter of the fundamental and SHG beams after the 50 mm collimating lens.

$$D_{SHG} = \left(\frac{4M^2\lambda}{\pi}\right) \times \left(\frac{F}{2w_{SHG}}\right)$$

$$= \left(\frac{4 \times 1.4 \times 1200 \times 10^{-6}}{\pi}\right) \times \left(\frac{50}{50 \times 10^{-3}}\right)$$

$$\approx 1.5 \text{ mm}$$

$$D_{\text{fundamental}} = \left(\frac{4M^2\lambda}{\pi}\right) \times \left(\frac{F}{2w_0}\right)$$

$$= \left(\frac{4 \times 1.4 \times 1200 \times 10^{-6}}{\pi} \right) \times \left(\frac{70}{50 \times 10^{-3}} \right)$$

$$\approx 1 \text{ mm}$$

After focusing using the 200 mm lens at the entrance slit, the diameter of the SHG beam at the slit will be:

$$2w_{SHG}' = \left(\frac{4M^2\lambda}{\pi} \right) \times \left(\frac{F}{D} \right)$$

$$= \left(\frac{4 \times 1.4 \times 1200 \times 10^{-6}}{\pi} \right) \times \left(\frac{200}{1} \right) \text{ mm}$$

$$\approx 290 \text{ } \mu\text{m}$$

And the diameter of the fundamental beam at the slit will be:

$$2w_0' = \left(\frac{4M^2\lambda}{\pi} \right) \times \left(\frac{F}{D} \right)$$

$$= \left(\frac{4 \times 1.4 \times 1200 \times 10^{-6}}{\pi} \right) \times \left(\frac{200}{1.5} \right) \text{ mm}$$

$$= 200 \text{ } \mu\text{m}$$

A4. Wavelength Dependent Efficiency Curve of CCD and Grating

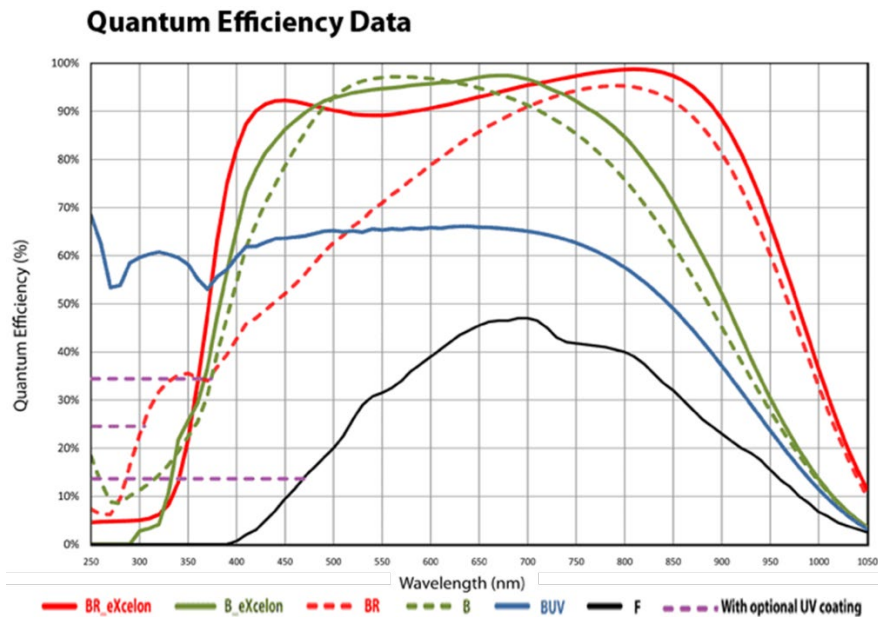


Figure A4.1. Quantum Efficiency of CCD: The wavelength dependent quantum efficiency curve of Teledyne Princeton PIXIS 1024B CCD (olive green dotted curve).

Source: www.princetoninstruments.com/products/pixis-family/pixis

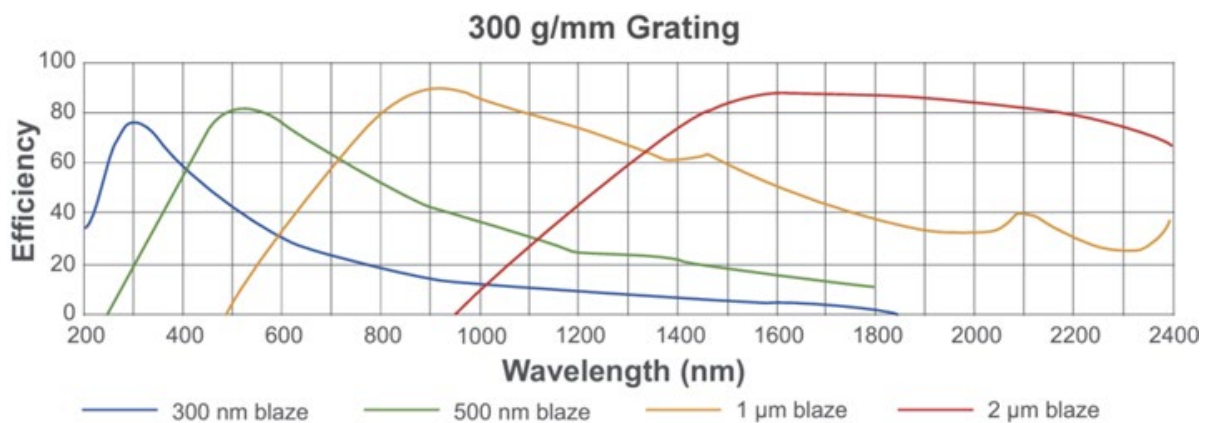


Figure A4.2. Efficiency of Diffraction Grating: The wavelength dependent efficiency curve of 300g/mm 500 nm blaze grating in Teledyne Princeton SpectraPro HRS300 spectrograph (green curve).

Source: www.princetoninstruments.com/products/spectrapro-family/spectra-pro-hrs

References

1. Ashcroft, N. W.; Mermin, N. D., *Solid State Physics*; Cengage Learning, 2022.
2. Bloch, F., Über Die Quantenmechanik Der Elektronen in Kristallgittern. *Z. Phys.* **1929**, *52*, 555-600.
3. Mendelson, B., *Introduction to Topology: Third Edition*; Dover Publications, 2012.
4. Hasan, M. Z.; Moore, J. E., Three-Dimensional Topological Insulators. *Annu. Rev. Condens. Matter Phys.* **2011**, *2*, 55-78.
5. Bernevig, B. A.; Hughes, T. L.; Zhang, S.-C., Quantum Spin Hall Effect and Topological Phase Transition in HgTe Quantum Wells. *Science* **2006**, *314*, 1757-1761.
6. Fu, L.; Kane, C. L., Topological Insulators with Inversion Symmetry. *Phys. Rev. B* **2007**, *76*, 045302.
7. König, M.; Wiedmann, S.; Brüne, C.; Roth, A.; Buhmann, H.; Molenkamp, L. W.; Qi, X.-L.; Zhang, S.-C., Quantum Spin Hall Insulator State in HgTe Quantum Wells. *Science* **2007**, *318*, 766-770.
8. Hsieh, D.; Qian, D.; Wray, L.; Xia, Y.; Hor, Y. S.; Cava, R. J.; Hasan, M. Z., A Topological Dirac Insulator in a Quantum Spin Hall Phase. *Nature* **2008**, *452*, 970-974.
9. Hasan, M. Z.; Kane, C. L., Colloquium: Topological Insulators. *Rev. Mod. Phys.* **2010**, *82*, 3045-3067.
10. Vafek, O.; Vishwanath, A., Dirac Fermions in Solids: From High-Tc Cuprates and Graphene to Topological Insulators and Weyl Semimetals. *Annu. Rev. Condens. Matter Phys.* **2014**, *5*, 83-112.
11. Kong, D.; Cui, Y., Opportunities in Chemistry and Materials Science for Topological Insulators and Their Nanostructures. *Nat. Chem.* **2011**, *3*, 845-849.
12. Armitage, N. P.; Mele, E. J.; Vishwanath, A., Weyl and Dirac Semimetals in Three-Dimensional Solids. *Rev. Mod. Phys.* **2018**, *90*, 015001.

13. Pal, P. B., Dirac, Majorana, and Weyl Fermions. *Am. J. Phys.* **2011**, *79*, 485-498.
14. Kumar, N.; Guin, S. N.; Manna, K.; Shekhar, C.; Felser, C., Topological Quantum Materials from the Viewpoint of Chemistry. *Chem. Rev.* **2021**, *121*, 2780-2815.
15. Soluyanov, A. A.; Gresch, D.; Wang, Z.; Wu, Q.; Troyer, M.; Dai, X.; Bernevig, B. A., Type-II Weyl Semimetals. *Nature* **2015**, *527*, 495-498.
16. Bansil, A.; Lin, H.; Das, T., Colloquium: Topological Band Theory. *Rev. Mod. Phys.* **2016**, *88*, 021004.
17. Chen, Y. L., et al., Experimental Realization of a Three-Dimensional Topological Insulator, Bi₂Te₃. *Science* **2009**, *325*, 178-181.
18. Peng, L.; Yuan, Y.; Li, G.; Yang, X.; Xian, J.-J.; Yi, C.-J.; Shi, Y.-G.; Fu, Y.-S., Observation of Topological States Residing at Step Edges of WTe₂. *Nat. Commun.* **2017**, *8*.
19. Wang, S.; Lin, B.-C.; Wang, A.-Q.; Yu, D.-P.; Liao, Z.-M., Quantum Transport in Dirac and Weyl Semimetals: A Review. *Adv. Phys.: X* **2017**, *2*, 518-544.
20. Boyd, R. W., *Nonlinear Optics*, 2020.
21. Shen, Y. R., Optical Second Harmonic Generation at Interfaces. *Annu. Rev. Phys. Chem.* **1989**, *40*, 327-350.
22. Hsieh, D.; McIver, J. W.; Torchinsky, D. H.; Gardner, D. R.; Lee, Y. S.; Gedik, N., Nonlinear Optical Probe of Tunable Surface Electrons on a Topological Insulator. *Phys. Rev. Lett.* **2011**, *106*, 057401.
23. Zong, A.; Nebgen, B. R.; Lin, S.-C.; Spies, J. A.; Zuerch, M., Emerging Ultrafast Techniques for Studying Quantum Materials. *Nat. Rev. Mater.* **2023**, *8*, 224-240.
24. Patankar, S., et al., Resonance-Enhanced Optical Nonlinearity in the Weyl Semimetal TaAs. *Phys. Rev. B* **2018**, *98*, 165113.
25. Lu, B.; Sayyad, S.; Sánchez-Martínez, M. Á.; Manna, K.; Felser, C.; Grushin, A. G.; Torchinsky, D. H., Second-Harmonic Generation in the Topological Multifold Semimetal RhSi. *Phys. Rev. Res.* **2022**, *4*, L022022.

26. Brown, B. E., The Crystal Structures of WTe_2 and High-Temperature $MoTe_2$. *Acta Crystallogr.* **1966**, *20*, 268-274.
27. Sie, E. J., et al., An Ultrafast Symmetry Switch in a Weyl Semimetal. *Nature* **2019**, *565*, 61-66.
28. Nakatsuji, S.; Kiyohara, N.; Higo, T., Large Anomalous Hall Effect in a Non-Collinear Antiferromagnet at Room Temperature. *Nature* **2015**, *527*, 212-215.
29. Higo, T.; Qu, D.; Li, Y.; Chien, C. L.; Otani, Y.; Nakatsuji, S., Anomalous Hall Effect in Thin Films of the Weyl Antiferromagnet Mn_3Sn . *Appl. Phys. Lett.* **2018**, *113*, 202402.
30. Mauck, M., Knife-Edge Profiling of Q-Switched Nd:Yag Laser Beam and Waist. *Appl. Opt.* **1979**, *18*, 599-600.
31. Born, M.; Wolf, E., *Principles of Optics: Electromagnetic Theory of Propagation, Interference and Diffraction of Light*; Elsevier, 2013.
32. Jiang, Y. C.; Gao, J.; Wang, L., Raman Fingerprint for Semi-Metal WTe_2 Evolving from Bulk to Monolayer. *Sci. Rep.* **2016**, *6*, 19624.
33. Reichlova, H., et al., Imaging and Writing Magnetic Domains in the Non-Collinear Antiferromagnet Mn_3Sn . *Nat. Commun.* **2019**, *10*, 5459.
34. Markou, A.; Taylor, J. M.; Kalache, A.; Werner, P.; Parkin, S. S. P.; Felser, C., Noncollinear Antiferromagnetic Mn_3Sn Films. *Phys. Rev. Mater.* **2018**, *2*, 051001.
35. Patterson, A. L., The Scherrer Formula for X-Ray Particle Size Determination. *Phys. Rev.* **1939**, *56*, 978-982.
36. Cao, Y.; Sheremetyeva, N.; Liang, L.; Yuan, H.; Zhong, T.; Meunier, V.; Pan, M., Anomalous Vibrational Modes in Few Layer WTe_2 Revealed by Polarized Raman Scattering and First-Principles Calculations. *2D Mater.* **2017**, *4*, 035024.
37. Abdol, S. O.; Abdollahipour, B., Asymmetrical Plasmonic Absorber and Reflector Based on Tilted Weyl Semimetals. *Sci. Rep.* **2021**, *11*, 15433.
38. Raether, H., Light Scattering at Rough Surfaces without an ATR Device. Springer Berlin Heidelberg: 1988; pp 73-90.

39. Bosshard, C.; Gubler, U.; Kaatz, P.; Mazerant, W.; Meier, U., Non-Phase-Matched Optical Third-Harmonic Generation in Noncentrosymmetric Media: Cascaded Second-Order Contributions for the Calibration of Third-Order Nonlinearities. *Phys. Rev. B* **2000**, *61*, 10688-10701.
40. Hu, X.-H.; Wei, F.; Wang, H.; Wang, H.-F., α -Quartz Crystal as Absolute Intensity and Phase Standard in Sum-Frequency Generation Vibrational Spectroscopy. *J. Phys. Chem. C* **2019**, *123*, 15071-15086.
41. Guan, M.-X.; Wang, E.; You, P.-W.; Sun, J.-T.; Meng, S., Manipulating Weyl Quasiparticles by Orbital-Selective Photoexcitation in WTe₂. *Nat. Commun.* **2021**, *12*, 1885.
42. Wen, X.; Gong, Z.; Li, D., Nonlinear Optics of Two-Dimensional Transition Metal Dichalcogenides. *InfoMat* **2019**, *1*, 317-337.
43. Khoo, I. C., Nonlinear Optics of Liquid Crystalline Materials. *Phys. Rep.* **2009**, *471*, 221-267.